Harlan, Jack Adair Jr. (Ph.D., Aerospace Engineering)

Short Time Scale Effects on High Frequency Radar-Derived Current Velocity Measurements

Thesis directed by Associate Professor Robert R. Leben

Recent efforts in the use of high frequency radar systems for near-real-time coastal ocean monitoring necessitate that short time scale motions of the radar-derived velocities are better understood. In the past, high frequency radar remote sensing of ocean currents has generally been limited to time scales of weeks to months. To obtain more reliable measurements at super-tidal frequencies, a new method, Empirical Mode Decomposition, is employed.

Our results indicate that wave field interactions account for a significant portion of the short time scale fluctuations that were previously attributed to inherent noise of the radar measurement. This provides better understanding of radar current measurements which will, in turn, provide better coastal monitoring.

CONTENTS

1. Introduction

The interaction of wind, waves and currents, especially on small time and space scales, has been the subject of increasing oceanographic research in recent years. Wind and wave interactions are important for better understanding of momentum and heat fluxes which are critical for modeling and forecasting both weather and climate. Locally wind-driven surface currents can often have magnitudes as large as the tidally-driven currents yet their dynamics, on temporal scales of hours and spatial scales of one to a few tens of kilometers, are not well understood.

Advances in both *in situ* and remote sensors have made possible higher sampling rates and greater spatial resolution which allow for the investigation of small-scale processes involving wind, waves and currents. One of these remote sensors, high frequency (HF) Doppler radars (HF: 3-30 MHz), have been used for measuring ocean surface currents since the 1970's (e.g., Barrick et al., 1977). They are unique in that their backscattered signal contains readily quantified information about 1) the two-dimensional surface wind field, 2) the surface currents and 3) the surface wave spectrum. These radars have primarily been used for measuring surface currents in coastal regions to understand coastal circulation on time scales of weeks to months. There has also been an ongoing effort to invert the backscattered signal to obtain the ocean wave directional spectrum, originally proposed by Barrick (1972) and continuing most notably by Wyatt (e.g., Wyatt, 1990,1991,1995; Wyatt and Green, 2002).

Recently, there has been a concerted effort by various governmental agencies within the U.S. to create a network of coastal ocean observing systems for prediction and monitoring of coastal circulation, wave and wind conditions (e.g., Malone, 2001). These observing systems will integrate a variety of sensors including traditional coastal-based meteorological instruments, tide gauges, buoy-mounted current meters, wave sensors and meteorological instruments, as well as HF radars. Some of the tasks for these systems include short-term warning (e.g., for navigation), monitoring (e.g., oil spill tracking) and real-time data dissemination to the public. Therefore, an improved understanding of the measurements by HF radars on these short time and space scales is necessary.
Here, the intent is to investigate short time scale (< 12 hour duration or > tidal frequency) current velocities as measured by HF radar and the effects of long (longer than locally-generated wind waves) ocean waves, as well as winds, on them.

2. Background

2.1 Current Velocity Measurements and Waves

Modern current meters and acoustic Doppler current profilers (ADCPs) are typically positioned so as to avoid the effects of wave motion and wind drift currents. For current meters, that means locating them several meters below the ocean surface while ADCPs are typically oriented so that their returned signal is not backscattering from a volume too close to the surface. It has been shown that some current meters using a Savonius rotor sensor, for example, will erroneously record high current velocities because it responds to oscillatory wave motion (e.g., Emery and Thomson, 1997). When time series of such current meters are transformed to power spectra and compared with current meters that are more immune to wave motion (e.g., the Marsh-McBirney current meter with electromagnetic sensors having high sampling rates or the Anderaa paddle wheel type current meter), the Savonius rotor-derived spectra exhibit amplitudes that are nearly an order of magnitude higher at frequencies greater than about 4 cycles per day or time periods of less than 6 hours (4 cpd = 0.166 cph; $\log_{10}(0.166) = -0.78$) (Figure 2.1). A qualitatively similar spectrum will result from time series of current meters that do not sample frequently enough causing the wave orbital velocity to be aliased into the measured current velocity (e.g., Woodward et al. 1990). Whether because of the type of current meter used or because of the sampling frequency, wave motion can cause large amplitudes at high frequencies in current meter velocity spectra.

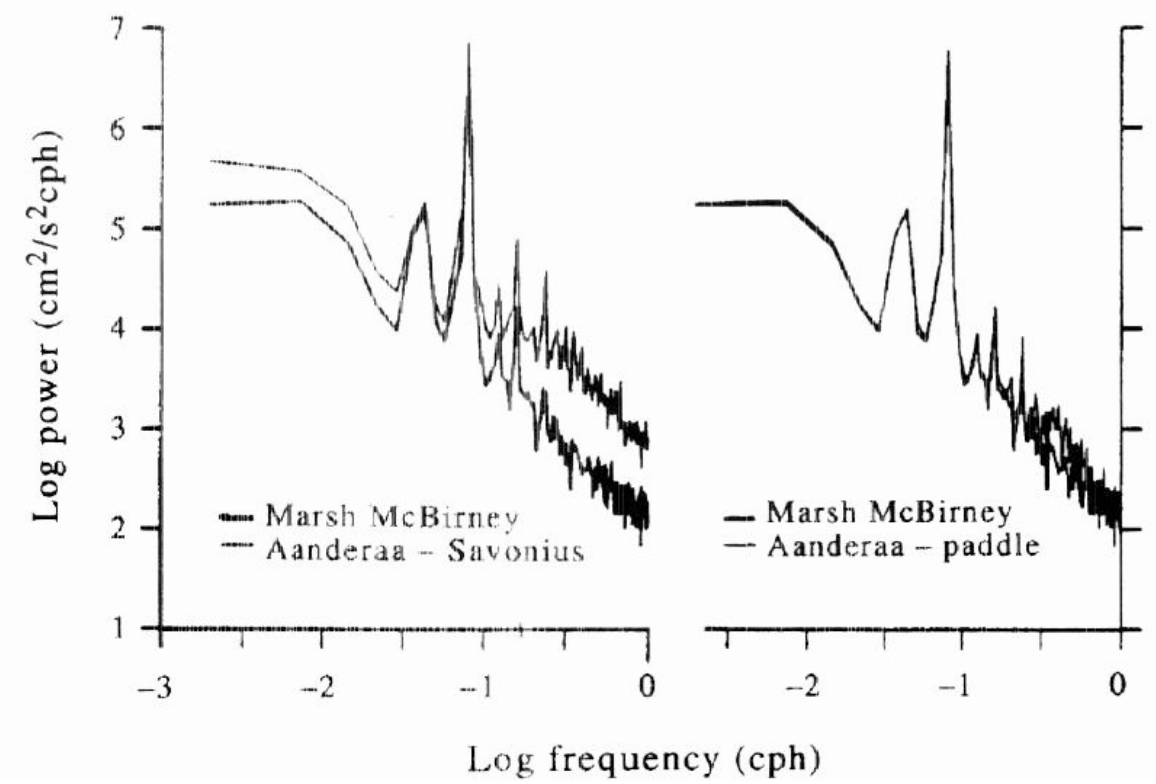

Figure 2.1 Spectra of Savonius Rotor versus Paddle Wheel relative to Marsh-McBirney Current Meter. From Woodward et al., 1990.

Richman et al. (1987) also demonstrated that the non-Savonius rotor current meters should not respond to surface wave motion when the standard averaging time of 60 seconds is used. For the proposed work, it is noted that a similar increase in amplitudes at frequencies greater than ~3 to 5 cpd exists for power spectra of HF-radar-derived velocities versus those from a non-Savonius rotor vector-measuring current meter (VMCM) (Figure 2.2). This pattern often exists for current meter moorings when compared with colocated radar data from HF radars that are currently deployed off the California coast.

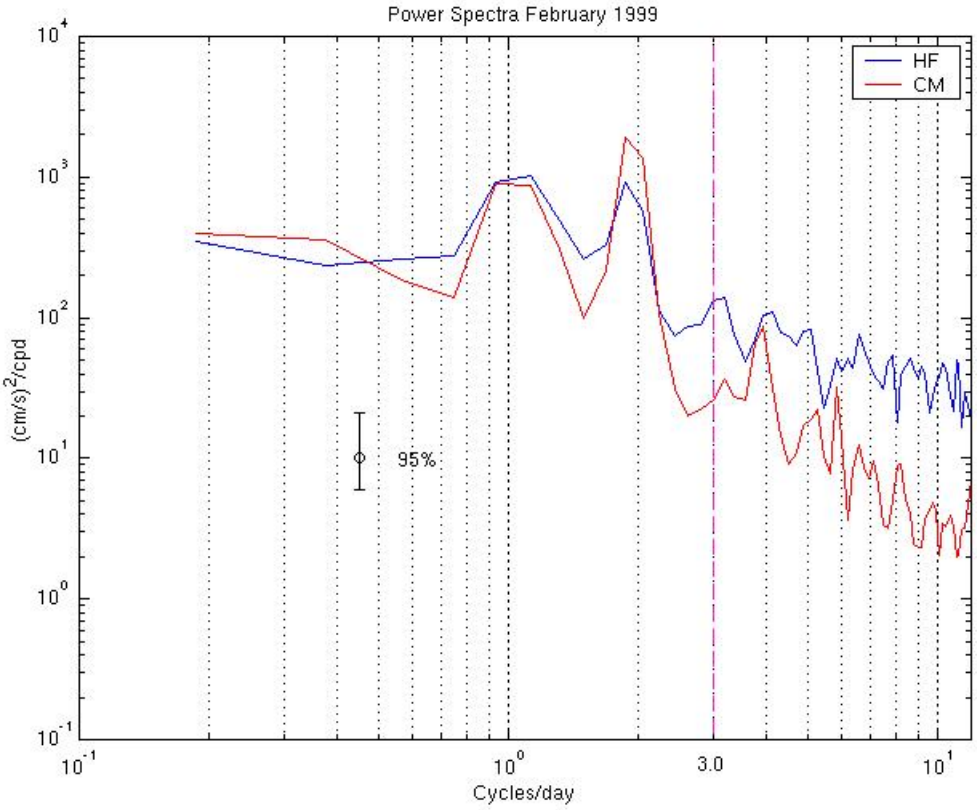

Figure 2.2 Frequency Spectra: VMCM and HF for Hourly Averages Feb 1999

In general, it is possible for a Fourier spectrum of a time series to exhibit incorrectly large high-frequency amplitude because of either a) non-stationarity or b) nonlinearity inherent in the time series. Because the Fourier transform is based on the presumption of linearity and stationarity, nonlinearity or non-stationarity is accommodated by inclusion of increasingly higher harmonics, up to the limit of the temporal resolution of the process. In the case of current velocity Fourier-based frequency spectra, these harmonics are manifested by abnormally large amplitudes at the higher frequencies, that is, the frequencies where the two spectra diverge. For the hour-long averages that comprised the time series from which the above spectra were created, short-time-scale intermittent motions, that are generally transparent to the current meters, may be one cause of the increased energy at higher frequencies.

Just as the Savonius rotor current meter could not distinguish between a current that was due to wave motion and a background current, an HF radar cannot distinguish between a wave- or wind-induced current and the larger scale background current e.g., tidal current. Therefore, these wind- and wave-induced currents could account for some of the differences between HF radar and in situ velocity measurements from vector measuring current meters.

Elucidating the causes, since there are likely to be more than one, of the differences in the two measuring systems that might account for the differences at high frequencies (greater than ~3 to 5 cpd) is the subject of this investigation. Generally, the possible causes will fall within two groups: 1) wave-induced effects due to waves whose wavelengths are much longer than the Bragg-resonant waves and 2) wind-induced effects due to the direct effect of the wind on the horizontal surface momentum.

2.2 HF Radar Current Mapping

Ocean current mapping HF radars transmit electromagnetic radiation that backscatters from ocean waves that are one-half the wavelength of the transmitted wave, i.e. Bragg scattering. Depending on the radar transmit frequency, the backscattering ocean waves are 5 to 50 m wavelength. In practice, frequencies of about 5, 12 and 25 MHz are used, which correspond to ocean wavelengths of 30, 12.5 and 6 m, respectively. These waves are created by the local winds and only propagate distances *O*(10 km) in contrast to ocean swell waves that can propagate distances *O*(1000 km). The magnitude of the 1st order Bragg peaks is dependent on the number of scatterers, i.e., Bragg-resonant waves, within the backscattering region.

Range resolution is accomplished by modulating the transmit frequency of the radar, usually a simple linear ramp over a small bandwidth, called a "chirp". This allows nearly continuous transmission, rather than switching on-off, as in a pulsed radar. Thus, these radars are FM-CW (frequency modulation, continuous wave) or FM-ICW (frequency modulation, interrupted continuous wave) when there is a very brief delay between chirps.

Maximum range is dependent on transmit power but more importantly, on external radio frequency interference (RFI). RFI may have a number of sources, simultaneously, e.g., galactic noise, man-made radio transmissions and lightning. These can all act to degrade the signal-to-noise ratio (SNR) in the Doppler spectrum.

The depth over which an HF radar measures current velocity is dependent on the wavelength of the Bragg-resonant waves. This is because the orbital velocity of an ocean wave acts upon depth in a manner that is directly proportional to the wavelength. Therefore, the depth of the underlying current that is advecting the Bragg-resonant waves must be the same or less than the depth of the waves' orbital velocity motion. The details of the vertical shear with the upper layers of the ocean will also influence the depth of the current measurement. In summary, lower radar frequencies (longer Bragg-resonant waves) will result in current velocity measurements over deeper depths. For the radar frequencies in use for this study, the depth over which the HF measurements are integrated is approximately 1 m.

By employing the linear dispersion relation, assuming deep water, the precise phase velocity is known and, in turn, the Doppler shift of the backscattered signal is pre-determined. Deviations from this phase velocity-induced shift are due to currents underlying the waves. The velocity resolution is dependent on the radar transmit frequency and the sampling time for each spectrum. For the systems used here, the resolution is approximately 0.04 m/s.

Currently, HF radars are designed and built as either a linear phased-array narrow beam system or a compact crossed-loop broad beam system. Narrow beam radar systems are more familiar to most people since they essentially "aim" their antenna to the area from which they receive their signal. The assumption is that the steering azimuth is known precisely and then the Doppler frequency is determined from the shift of the first-order Bragg peak. In the case of broad beam systems (Figure 2.3), it is assumed that the Doppler frequency is known precisely and the azimuth corresponding to that particular frequency shift (i.e., radial velocity) is then determined by using orthogonal antenna elements. This process is referred to as "direction-finding" (DF).

With narrow beam systems, each range cell is delineated by a range and azimuth, from which a Doppler spectrum, and thus a radial velocity, is obtained.

In contrast, the HF radars used in this study are DF systems: SeaSondes manufactured by Codar Ocean Sensors Ltd. These systems acquire only a single Doppler spectrum from each range and antenna element. Then, these spectra are processed at each range and a direction is assigned to each of the radial velocities indicated in the spectrum. The methods for accomplishing this processing are complex and their description is outside the scope of this thesis. It should be noted that the azimuthal resolution, then, is somewhat arbitrarily chosen for a DF system, since the algorithm can be parameterized to use any finite resolution.

Another relevant point of consideration for a DF system is that the ocean current field variability causes spreading of the Doppler spectrum which is necessary for the DF algorithm to perform properly. In the limit of a perfectly uni-directional current field having a velocity equal to the velocity resolution of the radar, e.g., 0.04 m/s, a current would be found at only one azimuth. So, it is important that the proper velocity resolution is chosen because it can determine the azimuthal coverage.

In the limit of very large currents and very large wave heights, it is possible that the spreading caused by each could result in overlapping of the first and second-order portions of the Doppler spectrum, making accurate velocity measurements impossible.

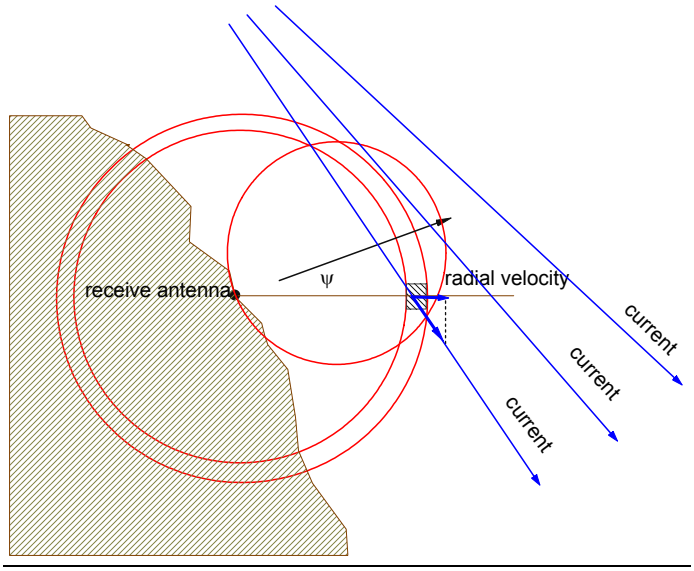

Figure 2.3 DF Radar Showing Range Ring Slice through Broad Beam

2.3. Previous Comparisons of HF Radar Measurements with In Situ Instruments

Comparing radar velocities with in situ measurements presents the classic problem of a point measurement versus a spatially-averaged measurement. Added to that difference is the vertical difference in the measurements. The radar measures surface velocity integrated over the upper meter or so (see the Background section) and the current meter measures at a particular depth. Over the past three decades, numerous comparisons have been made between the two types of measurements. Focusing on the most recent generation of HF radars, the reader is referred to comparisons that were explicitly reported (Graber et al., 1997; Chapman et al., 1997) and to comparisons presented in the context of a particular oceanographic study (Paduan and Rosenfeld, 1996; Kosro et al., 1997; Shay et al., 1998). Usually, the comparisons were made between vector velocities derived from two HF radars that simultaneously covered the same area and vector velocities from the current meter. To avoid the interpolation that is inherent in HF vector velocities, Emery et al. (2003) have compared the more direct measurement, radial velocities, with current meter vector velocities that are projected into the radial direction. For the present study, radial velocity will also be used.

Since the HF measurement is an integrated quantity over some area, variance of the current velocity field within that area will also lead to differences from the measurements of, say, a moored current meter within that area.

2.4 Waves and the HF Radar Signal

The ocean surface wave field is usually described in terms of a balance of three sources of energy, in the absence of currents: the wind input; nonlinear wave-wave interactions; and wave breaking. All of these processes interact to produce the wave directional spectrum which in turn affects the measurements of HF radars via the Doppler frequency spectrum. Two possible sources of wave-induced effects on the radar velocities are: 1) nonlinear wave-wave interactions which degrade the HF Doppler frequency spectrum, and 2) wave-induced motion that imparts a horizontal velocity to the surface, but is not measurable at the depths of most near-surface current meter moorings, and includes Stokes drift and wave breaking.

The theory for nonlinear wave effects on HF radar signals, as presented in Barrick, (1972) posits that these effects manifest themselves as significant peaks in the Doppler frequency spectrum (Figure 2.4). These are called “second-order” peaks since the nonlinear effects are of second-order in terms of the perturbation expansion used in the theory. The nonlinear effects are the result of the nonlinear wave-wave interaction that produces bound waves having the same wavelength as the Bragg-resonant waves and “double scattering” in which the radar signal reflection from two waves, at some angle to one another, happens to add in a way that a Bragg-resonant wavelength is formed. Because the resulting phase velocity of these nonlinear interactions may span a range of values, the second-order part of the Doppler spectrum is a continuum, not a specific peak. When the operating frequency for the radar is chosen appropriately, the second-order portion of the spectrum does not pose a problem. It has also been shown (Weber and Barrick, 1977; Barrick and Weber, 1977) that second-order wave-wave interactions cannot have the same phase speed as first-order Bragg-resonant waves and thus cannot cause Doppler shifts within the first-order region even though their wavelength may be equal to the Bragg-resonant waves.

However, when the Bragg-resonant waves are short relative to the predominant wave height (i.e., the chosen radar frequency is too high), the second-order portion of the spectrum can spread into the first-order region because of the transport of the smaller Bragg-resonant waves by the large waves. This creates an ambiguous boundary between the first and second-order portion of the spectrum which, in turn, can lead to erroneous estimates of current velocity by the particular spectral processing algorithm.

Specifically, if the rms wave height (rms wave height = significant wave height/($2\sqrt{2}$)) is less than $1/2k_o$ where k_o is the radar wavenumber, then second-order effects will not interfere with the first-order region (Barrick, 1986). For typical radar frequencies, 12.5 MHz and 25.4 MHz, the rms wave height

constraints are 2 m and 1 m, respectively, which correspond to significant wave heights of 5.4 and 2.7 m. The standard HF radar frequency of 12.5 MHz is effective for most of the Pacific coast of the United States, since significant wave heights, H_s, there exceed 5.4 m only occasionally. Furthermore, in practice, this is a conservative criterion. For example, during 4 April, 1999, an HF radar covered a region encompassing the Scripps Institution of Oceanography Harvest Buoy. The buoy indicated that H_s ranged from 5.42 to 6.57 m for approximately 7 hours (0200 to 0930 UTC), yet there was no leakage of the second-order portion of the spectrum into the first-order portion as seen in the plot of the Doppler frequency spectrum for 0500 UTC. There is still a well-defined "null" at 0.41 Hz that separates the 1st and 2nd order regions and the 2nd order peak is ~10 dB lower than the 1st order peak (Figure 2.4). Note that H_s had been 6.57 m at 0430 UTC.

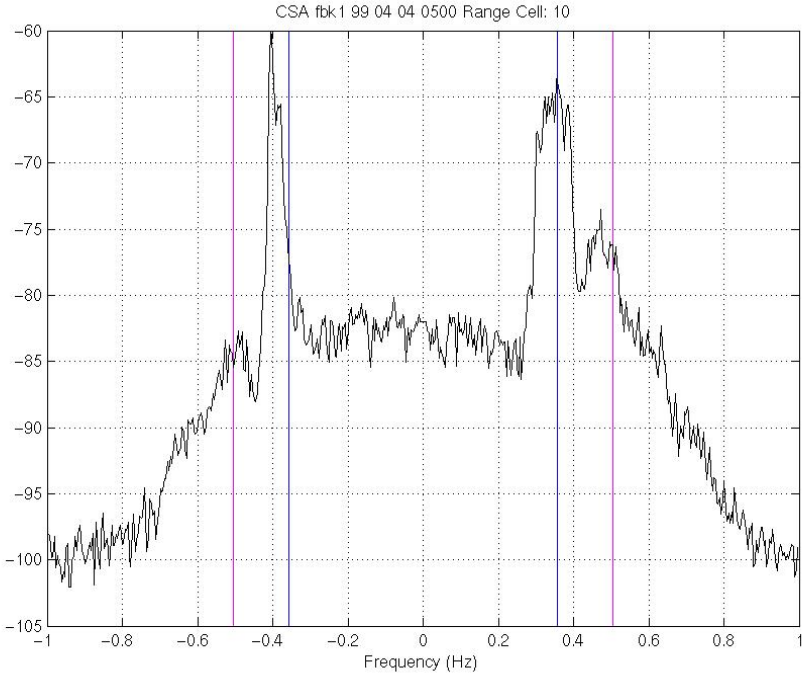

Figure 2.4 Doppler frequency spectrum during large SWH event. Blue line is frequency of theoretical 1st-order Bragg peak. Magenta line is frequency of theoretical 2nd-order "bound wave" peak.

2.5 Oceanic Wave Processes of Interest

Several processes that may cause short-time-scale motions in current velocities are explored below.

2.5.1 Stokes Drift and Wave-Induced Currents

Stokes drift is a result of the nonlinearity of an ocean surface wave. For ideal linear waves of infinitesimal amplitude, there is no Stokes drift. A realistic surface wave, having a finite amplitude, has a horizontal velocity in the direction of propagation whose speed is given by $u_s = a^2 k\omega$, where a is the wave height, k is the wavenumber and ω is the wave frequency. This movement in the direction of propagation is readily experienced by a swimmer who treads water just offshore of the surf zone and finds himself moving slowly toward shore with the passing of each successive wave. While the expression given above for a single wave is apparently simple, formulating an estimate for Stokes drift integrated over the nominal area observed by an HF radar has not been accomplished. It has been suggested (e.g, Madsen, 1978; Huang, 1979; Jenkins, 1987; Xu and Bowen, 1994) that one can simply

replace a^2 in the Stokes drift equation by the wave directional spectrum and integrate over wave frequency and wave direction. Of course, in practice, the wave directional spectrum is unknown. However, it can be estimated, e.g., by assuming one of the currently accepted forms such as the Pierson-Moskowitz spectrum (Pierson and Moskowitz, 1964; Madsen, 1978) or JONSWAP (Hasselmann et al., 1980) spectrum. When performing the integration it is necessary to restrict the upper limit of frequency such that it corresponds to the smallest waves whose restoring force is gravity, that is, to omit capillary waves.

The Stokes drift is usually defined to be effective over a depth, δ_e, equivalent to $1/(2k)$ where k is the ocean wavenumber (not to be confused with the $1/(2k_o)$ noted above, for the second-order effects of waves on radar backscatter where k_o is the radar wavenumber).

In addition to Stokes drift, there is a wave-induced current that is the result of viscosity, i.e., the Reynolds stress tensor and Earth's rotation. The original Stokes formulation was for invisid, irrotational flow. Over a century later, Ursell (1950) showed that, by retaining an inviscid flow but adding Earth's rotation in the equations of motion, that there could be no net wave-induced mass transport. Later, Longuet-Higgins (1953) revealed that there is, indeed, a wave-induced current when a small viscosity is applied to an irrotational wave flow. Surprisingly, this current diffused to the ocean layer below the surface and from the bottom layer to the intermediate depths. However, to model natural ocean conditions, both viscosity and rotation must be applied. This has been accomplished in both Lagrangian (Madsen, 1978; Weber, 1983; Jenkins, 1986; Weber and Melsom, 1993) and Eulerian (Huang, 1979; Xu and Bowen, 1994) coordinate systems. Among these models, there is agreement that the wave-induced current velocity is of the same order of magnitude as the wind-induced current, i.e., Ekman drift resulting from tangential wind stress.

By adding the wave-induced current derived from viscosity and rotation to the Stokes drift, these models estimate the entire current velocity due to properties of the wave field. However, all these models neglect the effects of wave breaking.

2.5.2 Wave Breaking

Wave breaking is a nonlinear process that occurs when a wave reaches a critical steepness. Wave breaking has several forms, e.g. spilling breakers that may or may not produce bubble-filled "white water", plunging breakers that have large splashes with much white water and microscale breakers that have no white water. One of the results of breaking is that momentum is lost from the wave and transferred to the ocean surface as a current velocity. This is clearly an intermittent process that is difficult to study under field conditions. Thus, the most detailed measurements have been in laboratory conditions. However, even these estimates, under carefully controlled conditions, have produced a wide range of results.

The mean drift current resulting from wave breaking has been found (when using a wire gauge technique in the laboratory) to be approximately $0.55u_*$, (e.g., Banner and Phillips, 1974) where u_* is the wind friction velocity. Later, Banner and Peirson (1998) estimated current velocities of $0.4u_*$ to $0.5u_*$ using particle image velocimetry techniques via neutrally buoyant spheres that reflect light from a sheet of laser light for accurate imaging of the air-water interface. The value of u_*/U_{10} is typically estimated as about 0.04-0.05 (e.g., Phillips et al., 2001) so that, for U_{10} ($O(10)$ m/s), the current velocity estimates of Banner and Peirson (1998) would be ~0.2 m/s. This is in agreement with previous laboratory measurements that indicate that a breaking-induced current velocity, normalized by the phase speed of the breaking wave in a fully developed sea, u_s/C, is about 0.02 (Rapp and Melville, 1990). So, for a typical breaking wave phase velocity, C, of 5 to10 m/s, u_s would be in the range 0.1 to 0.2 m/s. Another finding is that these current velocities persist for ~50 wave periods.

To take wave breaking into consideration for HF radar measurements, some estimate of spatial coverage of wave-breaking, as well as its duration, must be made. The statistics of wave-breaking is a topic of controversy since the choice of the wave height distribution is critical. The use of Gaussian statistics presumes that waves are a linear (or in some developments, weakly nonlinear) process, yet

wave-breaking is a strongly nonlinear process. Phillips (1985), derived a spatial distribution of wave-breaking assuming Gaussian statistics. However, Phillips' method requires the determination of several wind/wave-field dependent constants as well as the speed of the breaking event itself. Later, Srokosz (1986), used a distribution of maxima of a random function as applied to sea waves, but still based on Gaussian statistics, and found that the variance of the vertical acceleration of the sea surface height is the 4^{th} moment of the wave spectrum, m_4, can be used to compute the probability of breaking events.

Despite these attempts to estimate wave breaking probabilities, a review article of wave breaking (Banner and Peregrine, 1993), indicated that there was no field-tested, consensus method for estimating wave breaking statistics. And more recently, (Banner, Babanin and Young, 2000) the view is reiterated that no reliable method for estimating breaking wave statistics has been developed. This is followed with a comprehensive review of the present state of wave breaking statistics. However, Banner et al. then present evidence from three sets of field data that a parameterization of the significant wave steepness has a good correlation with wave breaking. This parameter is defined as $\varepsilon = H_p k_p/2$ where k_p is the wavenumber corresponding to the peak frequency of the wave spectrum and H_p is the significant wave height integrated over frequencies in the vicinity of the peak frequency. Thus, ε is an indication of the mean steepness of the dominant waves and also a measure of their nonlinearity. The steepness parameter was found to correlate, in a statistically significant way, with the occurrence of wave breaking after a threshold value was reached. A threshold should be expected since wave breaking is a nonlinear process and correlation is a linear one. So, the conclusion is that one can reliably expect wave breaking after a threshold of the steepness parameter is reached.

Recently, Melville and Matusov (2002) have examined whitecap coverage by analysis of video imagery taken from an aircraft at an altitude of approximately 400 m along a flight path of 15 km. They note that coverage ranges from about 0.5 to 1.5 % with fluctuations on scales of O(1-10) km. They also derive an empirical formula for the average length of breaking crests per unit area that has a dependence on $(U_{10})^3$. Furthermore, they show that breaking waves having phase velocities of 4 to 10 m/s (10 to 65 m wavelength) comprise most of the momentum flux and that the flux is primarily in the direction of the wind.

Given actual peak wave height and period data, the Banner et al, 2000 results can be used to estimate breaking probability. For the purposes of estimation of the extent of wave breaking as it relates to HF radar spatial coverage, assume a fully-developed sea state and the percentage of breaking as γ. Assuming deep water with typical values for HF radar range resolution of 1.5 km and an averaging time of 15 minutes for the radar, approximately γ % of 15 breaking events in space or 900/8 = 112 events in time could be sampled for a total of $15*112*\gamma$. Taking $\gamma = 5\%$ (a typical value found in the Banner et al., 2000 datasets), then the number of events would be 84 and the distance covered would be 84*4.5 or about 25% of the radar's range cell during the 15-minute averaging time. Clearly, this is a significant portion of the radar's cell.

The procedure for investigating wave effects on HF radar data will explore the Banner et al., 2000 findings for wave breaking spatial coverage. This will allow for estimating the potential effects of breaking waves on the HF-derived velocities.

3. Methodology

3.1 Data Description

The HF radar data consists of hour-long averages of radial velocity at spatial locations within the radar coverage areas of three Codar SeaSondes situated along the California coast, named FBK, ARG, RFG (Figure 3.1). The names are derived from the location: FBK for Fallback 22 on the Vandenberg Air Force Base, ARG for Pt. Arguello, RFG for Refugio State Park. Spatial coverage varies within the nominal coverage area of each radar, depending on the data quality at each point. Also, local

topographic features cause some blocking of the received signal at the two easternmost sites, so that the actual coverage is typically narrower in azimuth than that indicated in the plot.

Wind and wave data are also available within the Codar coverage areas. Two NOAA data buoys (46011 and 46023) each provide 10-minute averages of wind speed and direction in the vicinity of the open coastal radar coverages (FBK and ARG). They also provide wave non-directional spectral information. At the west and east ends of the Santa Barbara Channel which is near the farthest ranges of the RFG radar, the NOAA buoys 46054 (west) and 46053 (east) provide wind and wave data. At various times during 1999, there were moored current meters that were deployed by Scripps Institution of Oceanography within the coverage areas (AROF and SAOF). These current meters provided hourly current vector velocity averages at several depth levels, with the shallowest being 5 m. Finally, the Harvest buoy, providing wave directional spectrum data, is also present within the ARG radar coverage area.

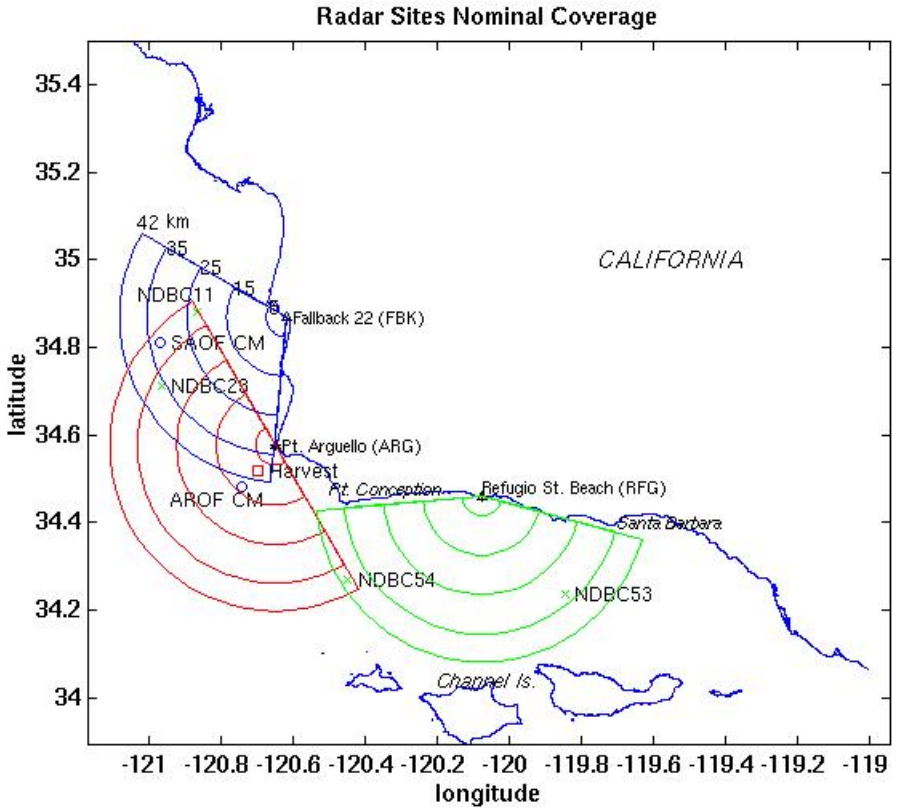

Figure 3.1 Coverage of the Three Radar Sites with Mooring Locations. Current Meters: "o"; NOAA Buoys: "x"; Harvest Buoy: square.

3.2 Data Analysis

Since the processes under consideration are intermittent in time and occur on short time scales, the primary method for analyzing the HF radar data time series is the empirical mode decomposition (EMD) (Huang et al., 1998). This method has some advantages over conventional Fourier spectral analysis. EMD is both data adaptive and local in its basis functions. In contrast, Fourier spectral analysis assumes an *a priori* form for the basis functions (i.e., trigonometric functions) and applies them globally to the entire data set. Additionally, Fourier analysis assumes linearity and stationarity of the time series. Assuming stationarity, in particular, is generally not warranted for the current velocity

time series that are under consideration here. In this respect, EMD has an advantage over Fourier analysis. The basis functions that comprise EMD, Fourier analysis, wavelet analysis and empirical orthogonal functions (EOF) are given in Table I.

	Local Basis Functions	**Global Functions**
A Priori Basis Functions	Wavelets	Fourier
Data Adaptive Basis Fns	EMD	EOF

Table I. Comparison of Basis Functions for Four Analysis Methods.

The EMD consists of an orthogonal set of functions that are derived from the data. These have been named "intrinsic mode functions (IMFs)" by Huang et al. (1998). The decomposition is complete, in that the original time series (Figure 3.2) can be reconstructed by simply summing the IMFs. An example of the IMFs for a month-long time series of hourly radial current velocities illustrates how the first IMF consists of the highest frequency motions, and the second, third and subsequent IMFs become less variable. Note also that the vertical scales are different for each IMF.(Figure 3.3)

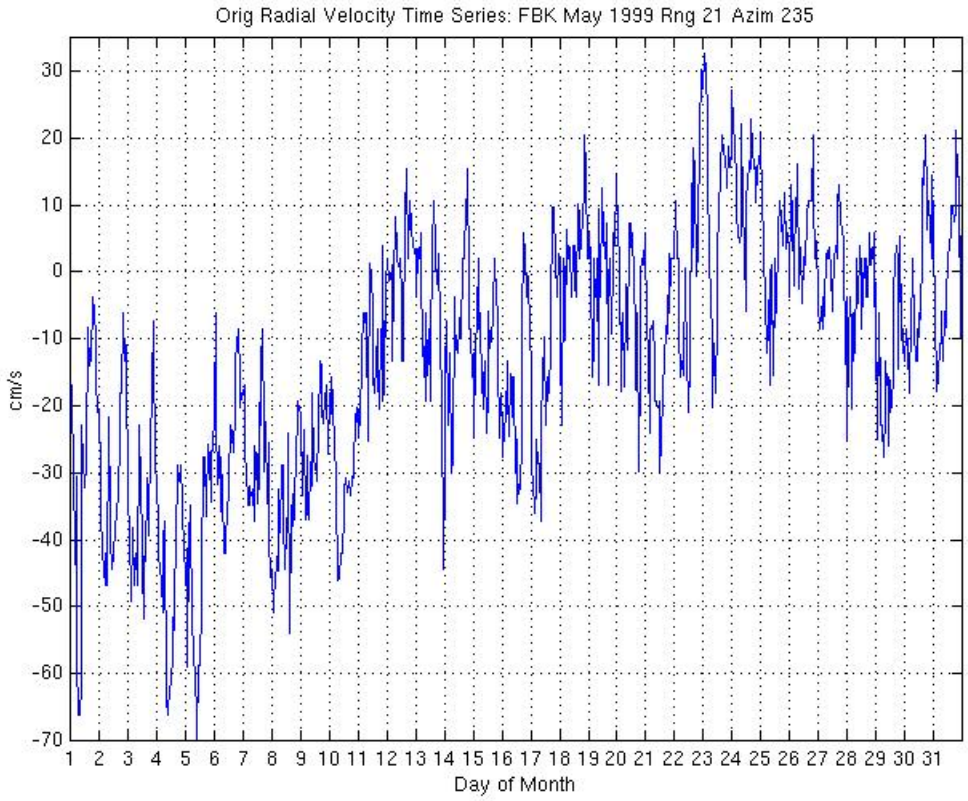

Figure 3.2 Example Original Time Series of Radar-Derived Current Radial Velocity

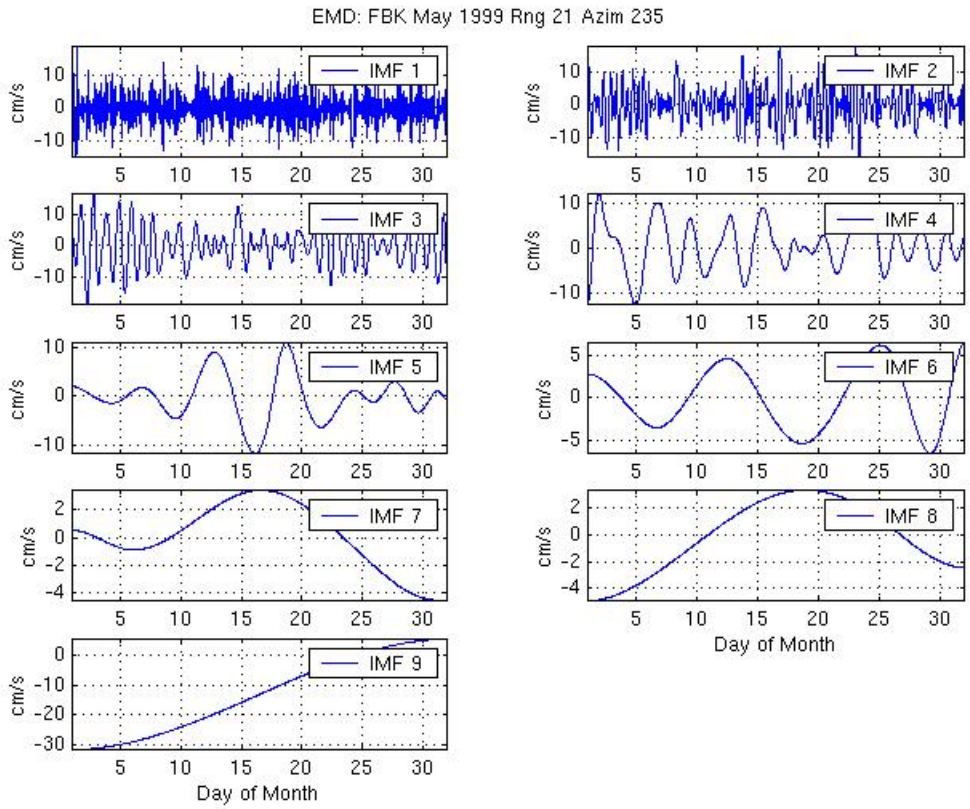

Figure 3.3 Eight IMFs from the Decomposition and Residual Trend (IMF9).

The algorithm for determining each IMF (or "mode") is as follows:

1). Define an initial trial function for the first IMF that is simply the original time series, itself H(t)

$h_{10}(t) = H(t)$ where the first subscript is the IMF mode number and the second subscript is the iteration index.

Find all local extrema. Connect the local maxima by a cubic spline curve. Do the same for the local minima.

Calculate the pointwise mean of the envelope constructed by the two splines.

2). Remove this mean, $m_0(t)$, from the initial trial IMF:

$$h_{11}(t) = h_{10}(t) - m_0(t)$$

3). Check for convergence of the IMF. Convergence is defined a priori as the iteration for which the absolute value of the difference of the current IMF and the previous IMF iteration is less than some small value.

Repeat Steps 1 and 2 as necessary using the nth trial function, $h_{1n}(t)$, for the next iteration

$$h_{1n}(t) = h_{1(n-1)}(t) = m_{n-1}(t)$$

4). At convergence, the first IMF, c_1, is given by the nth trial function

$$c_1 = h_{1n}$$

5). Define an initial trial function for the next IMF as

$$h_{(i+1)0}(t) = h_{i0}(t) - c_i(t),$$

and repeat Steps 1 to 4 until the IMFs 2 through N are found. At some iteration, the trial function will be strictly increasing or decreasing and have no local extrema on the interval. This is referred to as the "residual", r(t).

At this point, the original time series has been decomposed into a set of IMFs and a residual trend.

The first IMF (IMF1) contains the highest frequency motions of the time series. Therefore, IMF1 will be of the most interest for this study of short time-scale processes.

The intent is to examine both the statistics of IMF1 and the details of individual peaks within the IMF1 time series. As noted in the Data Description Section (Section 3.1), data from both low and high wave height time periods are available as well as areas where the wave height varies spatially. The expectation is that the statistics of IMF1 can give a quantitative indication of the presence of wave-induced effects. In addition, the details of the time series of an IMF1 can be compared with anomalous events that are revealed in the *in situ* wave data from the Harvest buoy.

4. EMD Application to Time Series of Colocated Current Meter and Radar-Derived Velocities

4.1 HF Radar Velocity Power Spectra

The conspicuous increase in spectral power levels for HF velocity spectra mentioned above have also been noted by Emery et al., 2003. Spectra of month-long hourly data time series for current meters and HF radar data are examined here. The radar data are averaged together when they are within 3 km of a current meter location. An example of a one-month-long time series for radar data in the vicinity of current meter SAOF for May 1999 is given in Figure 4.1, top panel. EMD is then applied to the time series and the time series is reconstructed with IMF1, the highest frequency mode, removed (Figure 4.1, bottom panel). The reconstructed time series is then transformed into a power spectrum and plotted over the original spectrum (Figure 4.2).

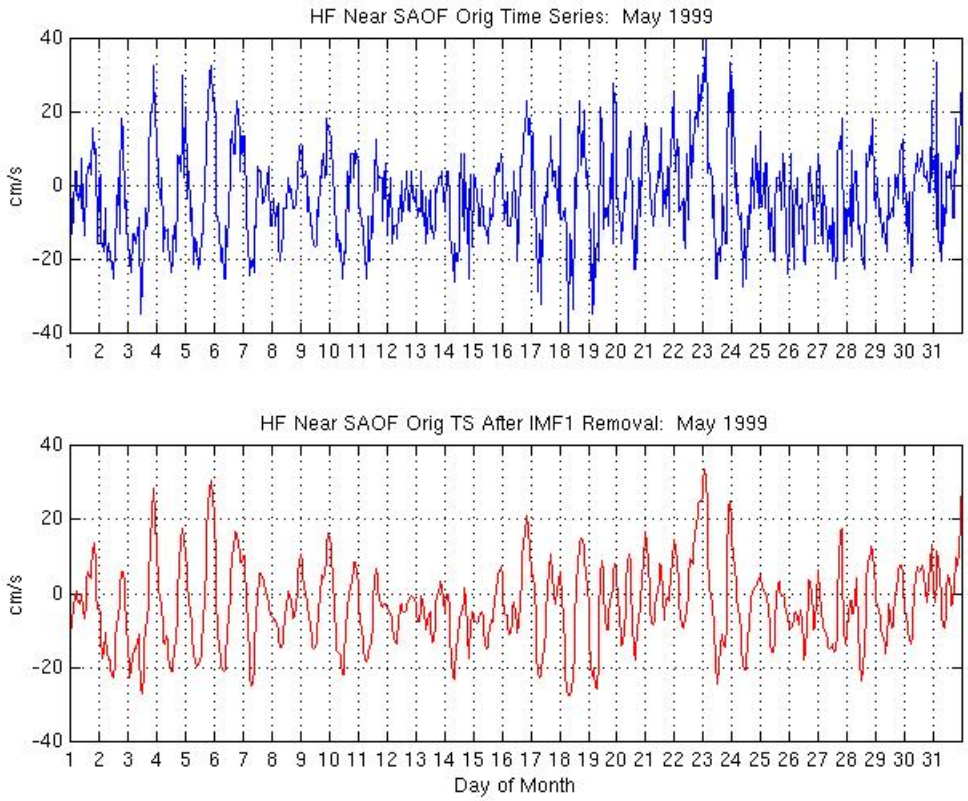

Figure 4.1 HF Original Time Series (top); HF Original Minus IMF1

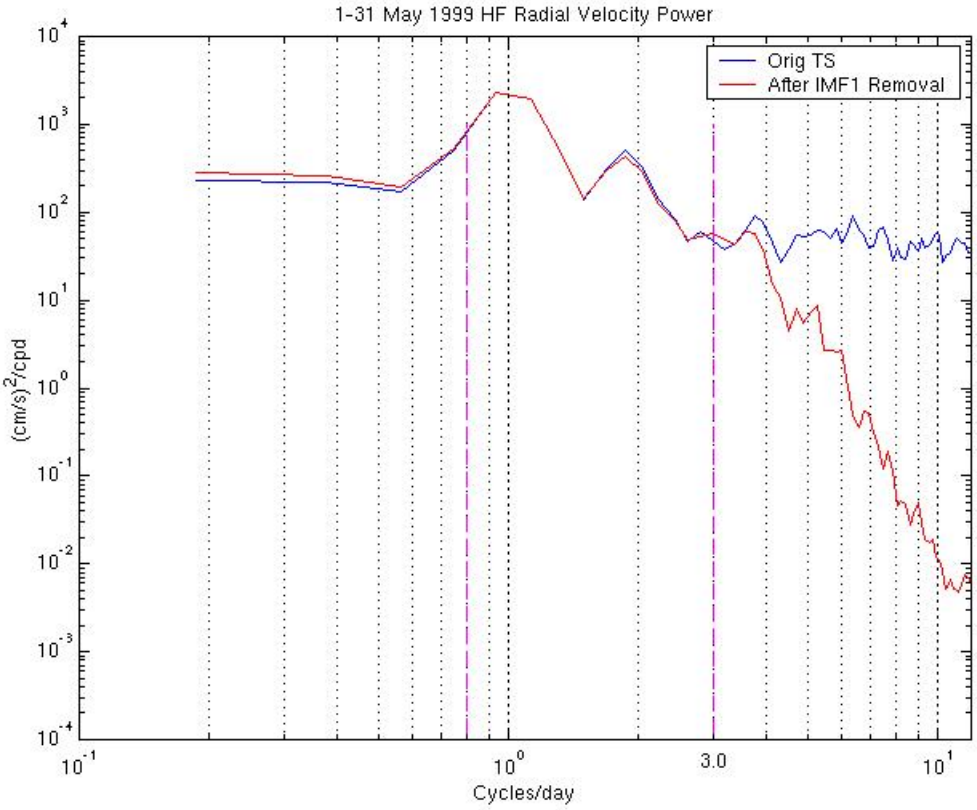

Figure 4.2 Example Power Spectra for Radar-Derived Velocity Time Series Before and After IMF1 Removal

The spectrum without IMF1 (red line in Figure 4.2) exhibits a steep decrease in power beginning about 3 to 4 cpd and continuing to the highest resolvable frequency (12 cpd). The ratio of power before/after the removal of IMF1 at frequencies greater than 3 cpd is approximately 6.30. However, the power at frequencies less than or equal to 2 cpd remains unaffected by the removal of IMF1: ratio of power is 1.04. Particularly, the dominant diurnal and semidiurnal tidal peaks are nearly unchanged. And, including all frequencies greater than 0.8 cpd, integrated power is reduced by 34% when IMF1 is removed from the time series.

Comparing the power spectra for the current meter (CM), HF radar (HF) and the HF radar time series minus IMF1 (HFM1) (Figure 4.3) and assuming that the CM represents physical "truth", it is seen that the HFM1 spectrum has lower energy at high frequencies than the CM. This suggests that HFM1 contains physically measurable (by the CM) motions. It further suggests that IMF1 may contain motions that are either measured only by the radar or are simply due to the instrument e.g. signal processing noise in the radar measurement, intrinsic hardware-related noise or some other non-oceanic phenomena.

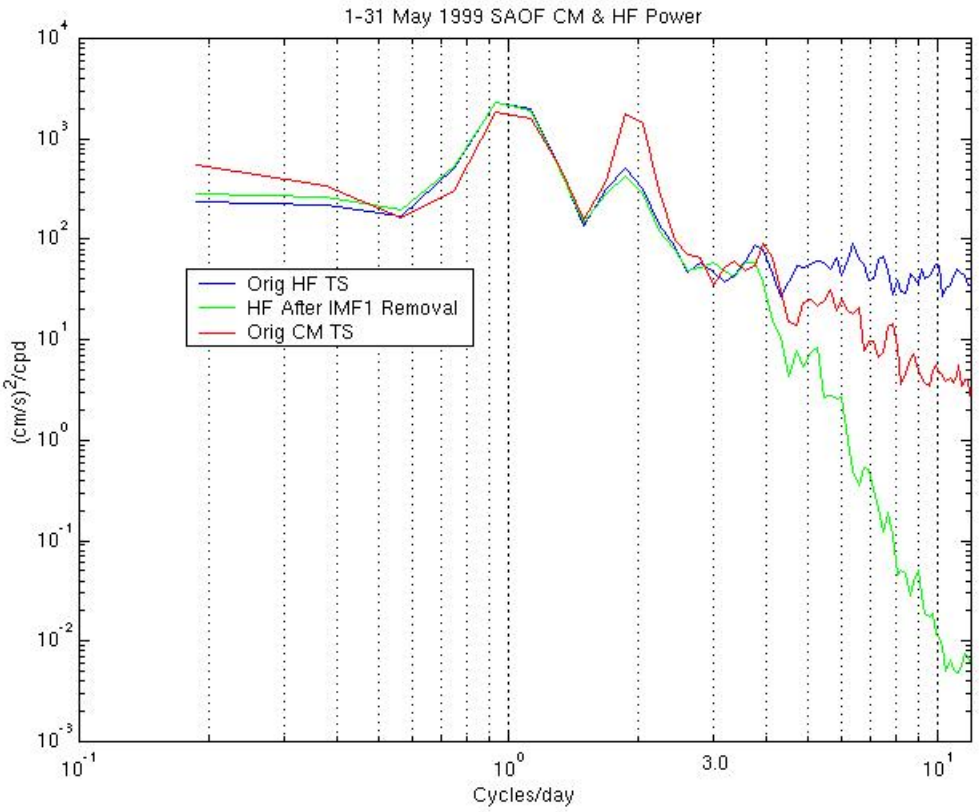

Figure 4.3 Example Power Spectra for Radar-Derived Velocity Time Series Before/After IMF1 Removal and CM Velocity Time Series

4.2 Current Meter Velocity Power Spectra

Applying EMD to the SAOF CM data May 1999 hourly time series, as for the HF radar data, gives seven intrinsic mode functions and a residual or "trend" function (Figure 4.4).

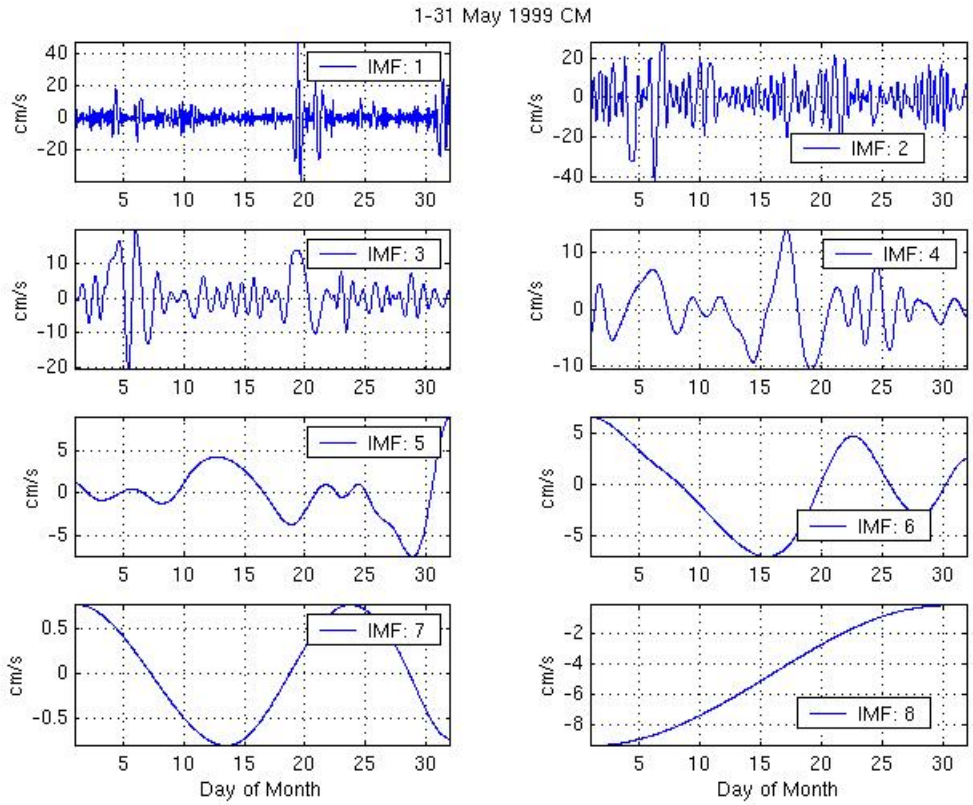

Figure 4.4 Intrinsic Mode Functions and Residual (IMF 8) of CM Velocity Time Series

In this example, it is apparent that IMF1 contains some motions that are anomalously large compared with the majority of IMF1 e.g. days 19 and 31 (Figure 4.5). This is a case of "mixed modes" or "intermittency" as defined in Huang et al. (1999). In other words, more than one physical mode is included in the particular IMF. Additionally, IMF1 is plotted with the original time series in order to illustrate the relative size of IMF1 compared with the complete radial velocity time series.

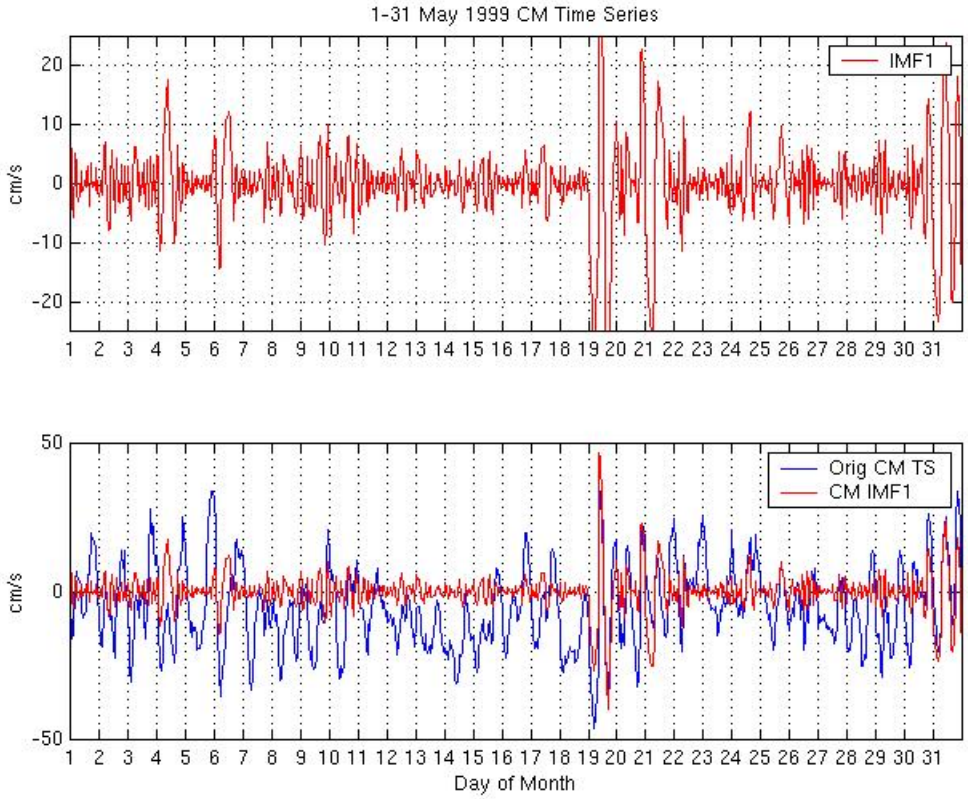

Figure 4.5 IMF1 (top) and IMF1 Overlaid on Original CM Time Series (bottom)

Following the same proceduare as for the HF data above, IMF1 is removed from the time series and the new time series is transformed to a power spectrum. The power spectra of the original time series (CM) and the time series minus IMF1 (CMM1) are plotted (Figure 4.6). There is a decrease in the power spectral tidal peaks after removal of IMF1 suggesting that IMF1 contains tidal motions. The even larger decrease at higher frequencies is also evident, consistent with the HFM1 spectrum.

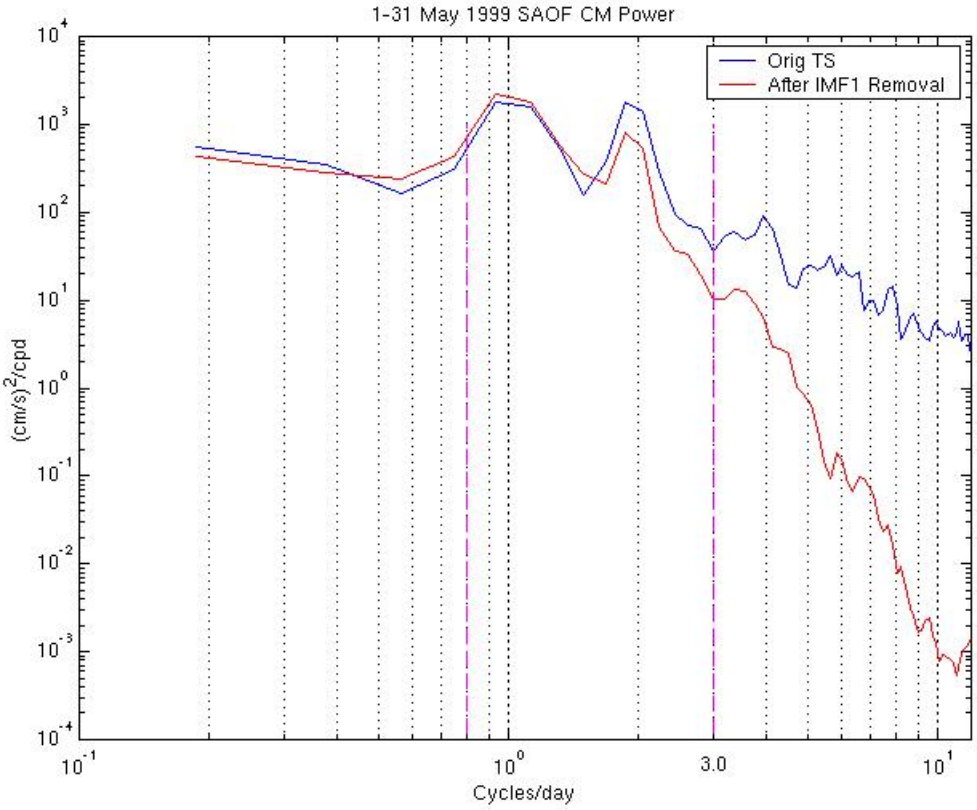

Figure 4.6 Power Spectra CM Before and After IMF1 Removal

Noting that the subset of the CM time series from day 7 through day 18 does not exhibit any anomalous peaks (Figure 4.5), EMD is applied to this data subset. IMF1 is removed from the subset time series and spectra for both the original subset and the subset without IMF1 are plotted (Figure 4.7). In contrast to the complete monthly time series spectra in Figure 4.6, the tidal peaks for the subset spectra are nearly unchanged. Therefore, it is concluded that IMF1 for the CM, in the absence of intermittency, contains only higher frequency motions i.e., motions that are super-tidal.

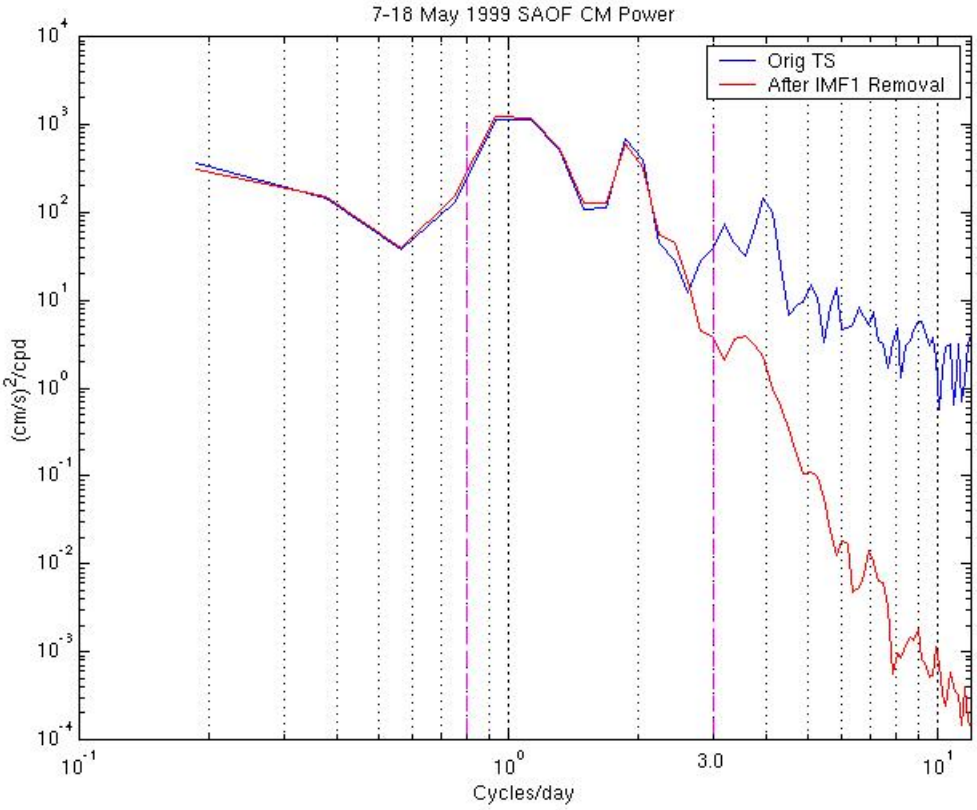

Figure 4.7 Power Spectra for Non-Intermittent CM Time Series

Finally, for the non-intermittent subset of the time series, the CM spectrum, the HF spectrum and the HFM1 spectrum are plotted in Figure 4.8. This illustrates that, for tidal frequencies, the HF and CM generally agree while at frequencies above about 3 to 5 cpd, the HF and CM spectra diverge. Additionally, after removing IMF1 from the HF data, the spectrum has much less energy than the CM indicating, as in the example above, that IMF1 includes some motions that are measured by the CM.

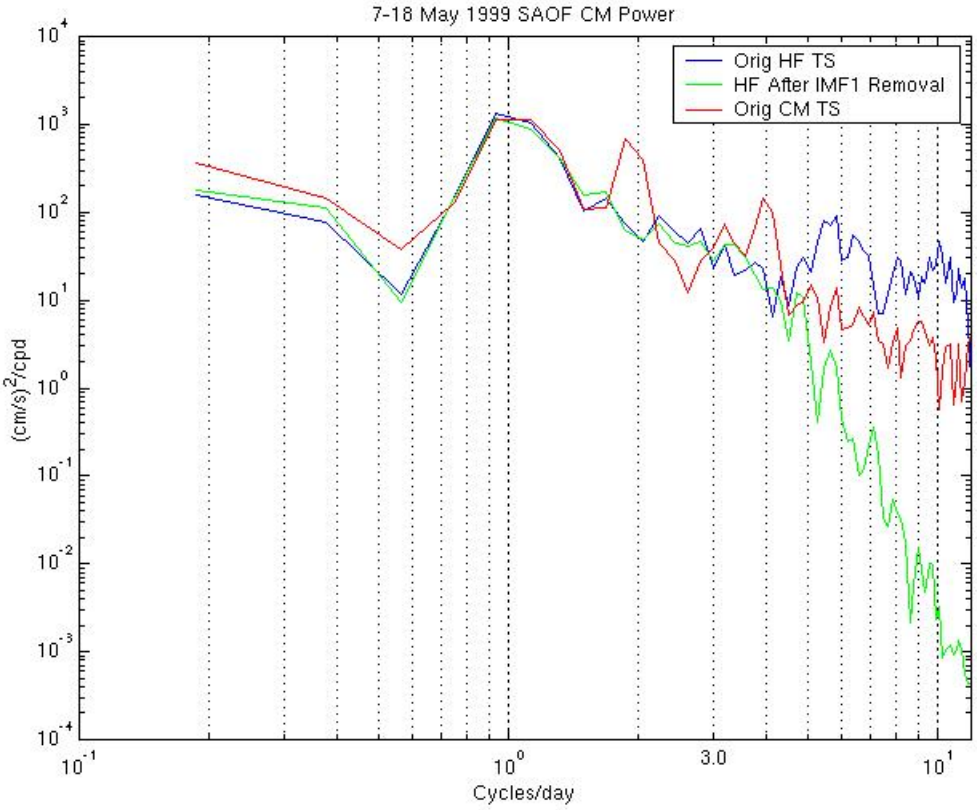

Figure 4.8 Power Spectra for HF, HF after IMF1 Removal, Non-Intermittent CM Time Series

4.3 Summary: Colocated CM and HF Radar Spectra Results

Several results are apparent after applying EMD to simultaneous, colocated measurements and removing IMF1.

1. HF radar-derived velocity spectra exhibit much greater energy at frequencies above about 3 to 5 cpd than does the CM.
2. After removal of IMF1 from an HF time series, HF spectra have *less energy* at frequencies greater than 3 to 5 cpd than do CM spectra.
3. The energy in the dominant tidal band (diurnal and semi-diurnal tides) is nearly unchanged after removing IMF1 from HF time series.
4. The energy in the dominant tidal band (diurnal and semi-diurnal tides) is nearly unchanged after removing IMF1 from CM time series, if IMF1 does not exhibit mixed modes.

These spatially-limited results persuade one to investigate further the behavior of IMF1 for more locations and times.

5. Spatial Distribution for IMF1 of HF Radial Velocities Time Series

Since this work is the first application of Empirical Mode Decomposition (EMD) to the analysis of HF radar radial velocities, a considerable effort has been expended to clarify the properties of EMD under a variety of geophysical conditions. The datasets used herein provide a view of open coastal areas (i.e., open directly to the Pacific Ocean with no topographic impediments to either wave or current actions) as well as regions within the more protected environment of the Santa Barbara Channel (SBC). Additionally, many months of data are available at each radar site so that a wide range of wind, wave and current conditions are included.

5.1 Methodology

For spatial distribution of the characteristics of IMF1, one-month-long time series of HF radial velocities were created from every point within the coverage area of the radar site. The nominal number of points at a radar site varies due to the azimuthal coverage of the radar. Each azimuthal bearing is 5 degrees wide and contains 28 range cells. At FBK, an open coastal site, the maximum azimuthal coverage is about 100 degrees or 21 separate bearings. This results in a maximum of 588 radar cells for each month at FBK. For convenience of processing, the EMD processing was confined to range rings 5 through 28 which still provide several hundred range cells during each month.

Originally in this study, EMD was performed only on month-long time series at radar cells that were in the vicinity of one of the VMCMs. IMF1 was then extracted from each decomposition and the standard deviation of each IMF1 was computed. We refer to the standard deviation of IMF1 from these month-long time series as “SI”. Initial results showed that the range of the SI values was quite small, e.g., from about 3 to 7 cm/s. To discern the complete two-dimensional distribution of IMF1, the next step was to perform EMD on every range cell of interest within the radar coverage areas and for multiple month-long time series.

Several questions were under investigation for these month-long time series:

1. Does IMF1 simply vary with the original radial velocity time series, i.e., do greater fluctuations in the radial velocities translate to greater values of the standard deviation of IMF1?
2. Does IMF1 vary with range away from the radar site? Radar SNR sometimes declines significantly within the nominal range coverage which would lead to more fluctuations in the measured radial velocity.
3. Since a filling technique is used to fill in missing values in the radial velocity time series, does IMF1 vary with the amount of filling that was performed?
4. What is the probability distribution of SI for various months and radar sites?
5. Does a month-long mean of SI vary with wind/sea state conditions?
6. Does IMF1 depend on radar operating frequency?

5.2 Background: Wind and Wave Conditions of the California Coast

Climatological records suggest that the California coastal region of Pt. Conception experiences its strongest winds (mean: 8 to 10 m/s) and largest significant wave heights (mean: 2.5 m) during the spring months of March, April and May. The smallest wave heights (mean: 1.6 m) are usually during late summer and early fall, i.e., August, September and October. Light winds are also associated with these autumn months (mean: 5 m/s) but occur for extended periods between meteorological frontal systems during the winter months, as well.

The Santa Barbara Channel (SBC), where the RFG radar site is located, usually has a strong decreasing gradient from west to east for both wind speed and wave height. Within the eastern part of the SBC, the wind speeds are relatively constant year-round with mean speeds as much as 6 m/s less than the western portion (mean: 4 to 5 m/s) and significant wave heights with mean of 1 to1.5 m.

With this historical information in mind, the spring months will be a focus of the investigation for large wind and waves and the autumn months of August and September will be referenced for the lighter wind and wave conditions.

5.3 Results

5.3.1 Results: Open Coastal Sites – High Wind and Wave Conditions

During April and May 1999, the significant wave height (H_s) was 2.5 m and 2.4 m, respectively, and was more than 3.0 m during 35% of April and 22% of May. The mean wind speeds in the vicinity of FBK during April and May 1999 were about 8 and 10 m/s, respectively. Additionally, during April and May 1999, winds greater than 10 m/s occurred during 35% and 54% of the month, respectively.

Spatial distribution maps of SI (Figure 5.1) at this open coastal site show that there is little spatial pattern. The questions above are, to a great extent, answered by the scatter plots (Figure 5.2). For each of the comparisons within the scatter plots, the correlation, r, is given. The plots and these correlations indicate that SI is not related to these parameters. There is, however, a small trend for increasing SI with range for the first 5 or so range cells.

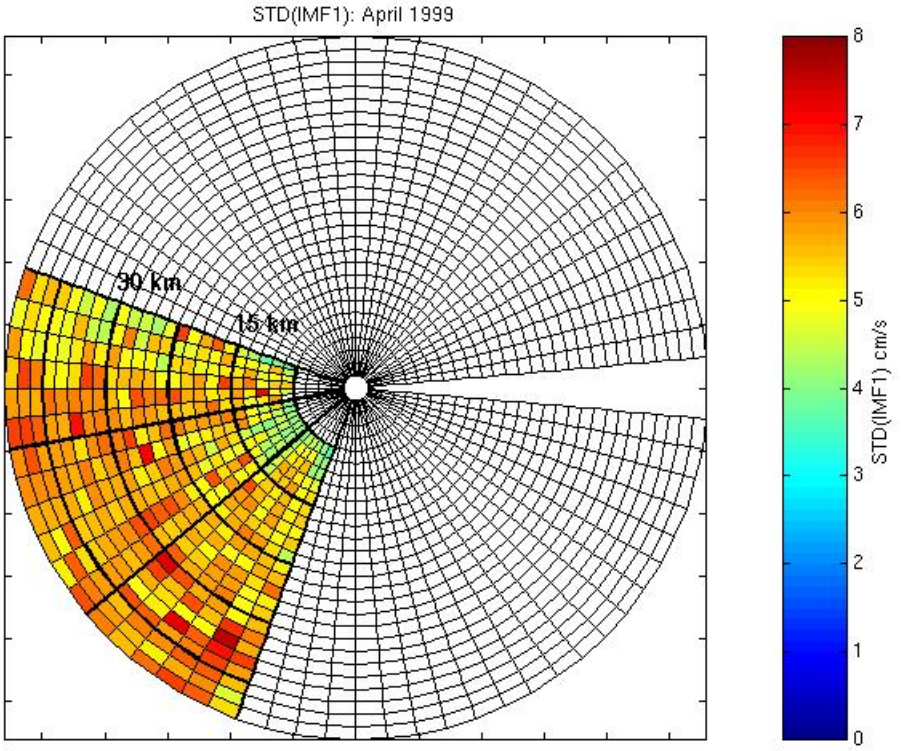

Figure 5.1 Coastal: SI Spatial Distribution in Range/Azimuth for April 1999. North toward top of plot.

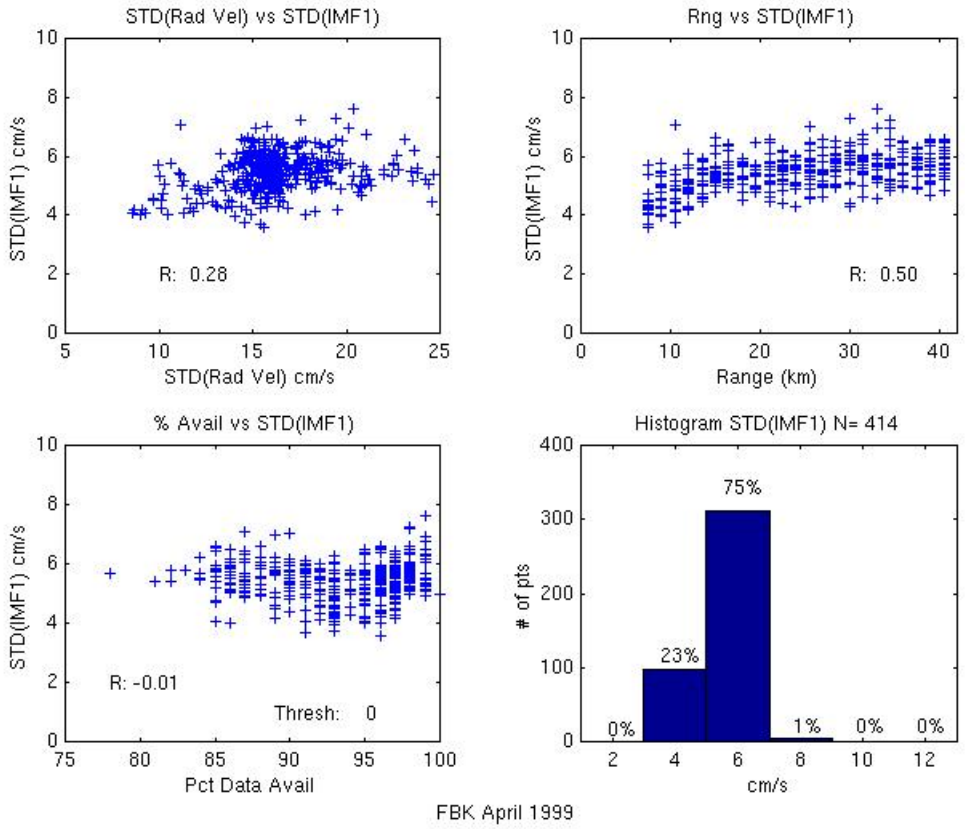

Figure 5.2 Coastal: April 1999 SI vs RadVel (UL); SI vs Range (UR); SI vs %Cov (LL) ; Histogram SI (LR)

5.3.2 Results: Open Coastal Sites – Low Wind and Wave Conditions

For the low wind and wave conditions of September 1999, mean wind speeds at NDBC11 and NDBC23 were 3.6 and 4.5 m/s, respectively, with winds greater than 10 m/s occurring only about 3% of the time. Significant wave heights were at NDBC11 and NDBC23 were 1.6 and 1.7 m, respectively. Although these wind/wave conditions were very different from April 1999, similar plots to the high wind/wave conditions are produced (Figure 5.3). The overall mean of SI is slightly higher than that of the high wind/wave conditions. The scatter plots also show similar patterns to those of the high wind/wave conditions. (Figure 5.4) Also, similar to the high wind/wave conditions, there is a small trend for increasing SI with range for the first several range cells.

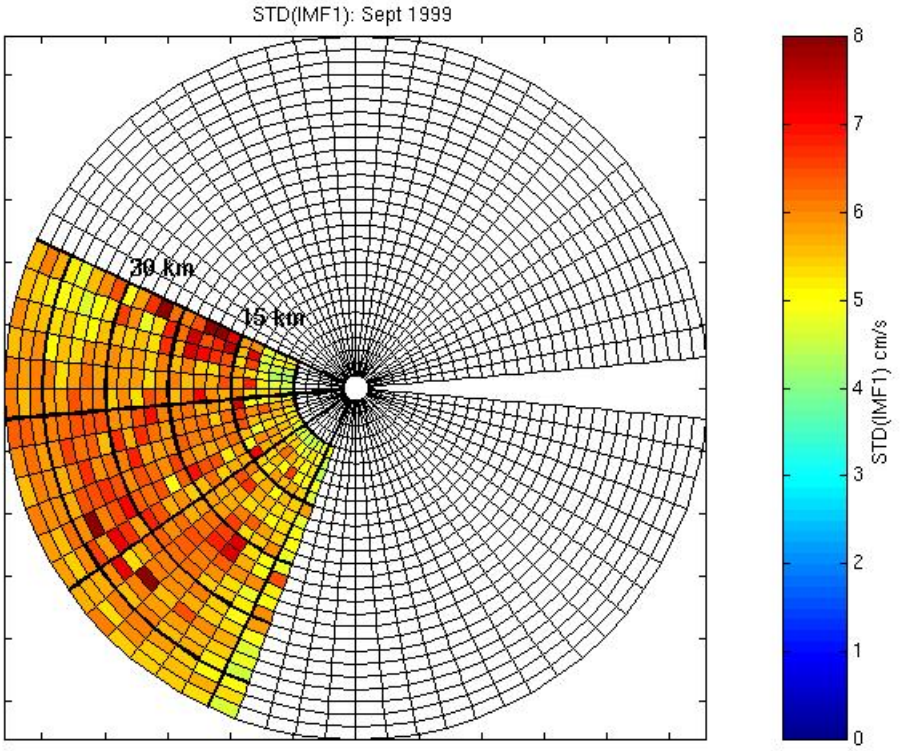

Figure 5.3 Coastal: SI Spatial Distribution in Range/Azimuth for Sept 1999. North toward top of plot.

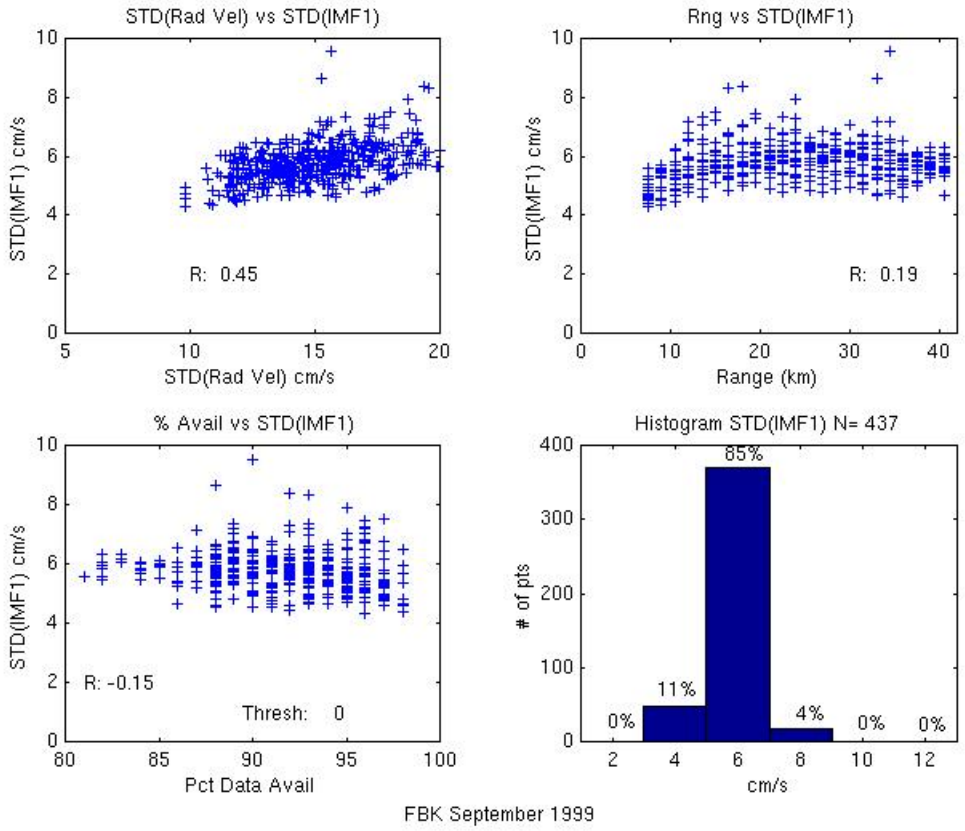

Figure 5.4 Coastal: Sep 1999 SI vs RadVel (UL); SI vs Range (UR); SI vs %Cov (LL); Histogram SI (LR)

5.3.3 Results: Santa Barbara Channel Sites – High Wind and Wave Conditions

The SBC site, RFG, presents a more complicated picture. Spatial distribution (Figure 5.5) and scatter plots (Figure 5.6) reveal apparent differences between these SBC sites and the open coastal sites. The most obvious difference is that there is a clear pattern of increasing SI with increasing range. This is seen in both the spatial maps and the scatter plots. The other difference is that the proportion of the distribution of smaller SI values (the 3 to 5 cm/s bin) in the histogram plots is greater for RFG than for the open coastal site. It is also notable from the spatial map that the values of SI are small for all azimuths for ranges less than about range cell 15 (22.5 km for the scatter plots). The transition to larger SI values occurs at about range 25 to 30 km and coincides with proximity to the lee side of the Channel Islands.

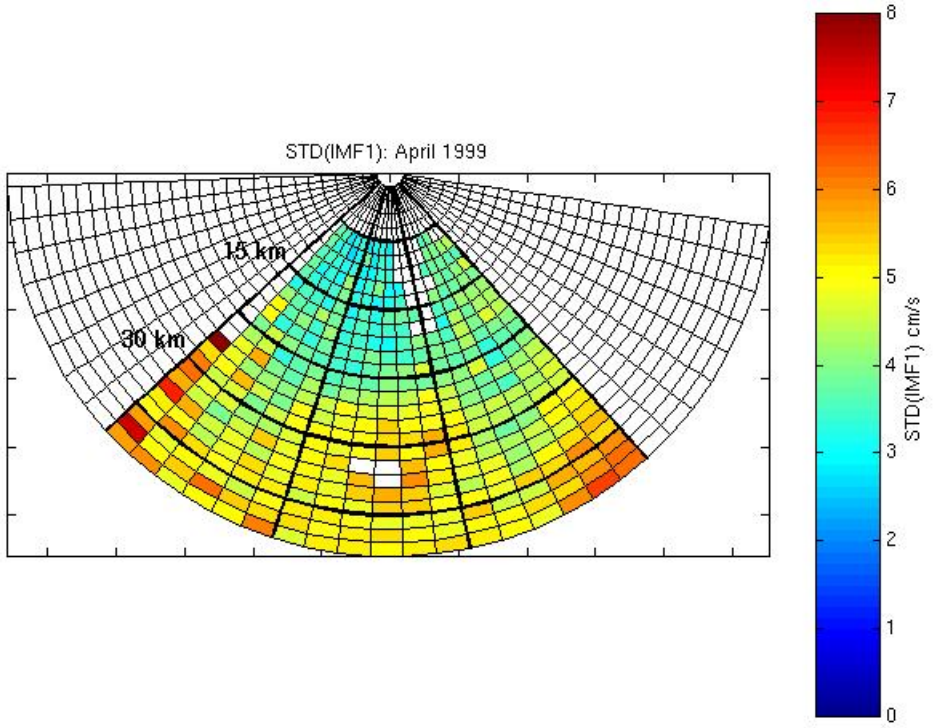

Figure 5.5 SBC: SI Spatial Distribution in Range/Azimuth for April 1999. White indicates missing data.

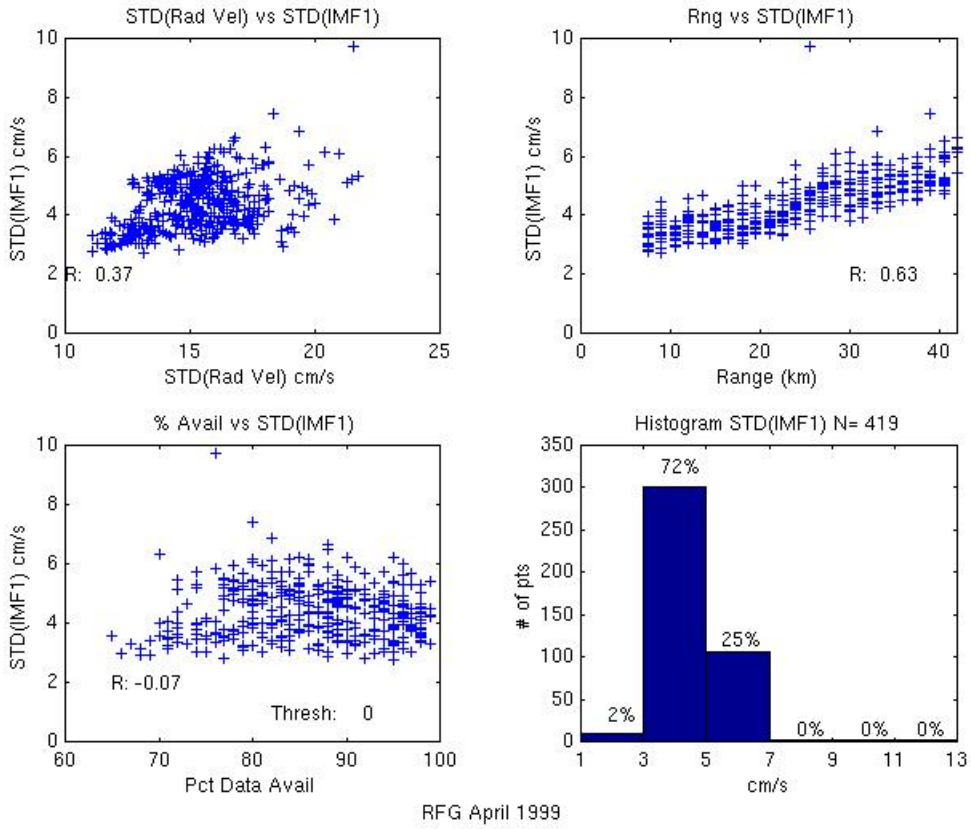

Figure 5.6 SBC: Apr 1999 SI vs RadVel (UL); SI vs Range (UR); SI vs %Cov (LL); Histogram SI (LR)

5.3.4 Results: Santa Barbara Channel Sites – Low Wave Conditions

Similar to the SBC high wind/wave conditions, the spatial map (Figure 5.7) and scatter plots (Figure 5.8) for September 1999 show a pattern of increasing SI values with increasing range and are significantly correlated. At the east end of the SBC, at NDBC53, the wind speeds (mean = 4.2 m/s) are significantly less than at the west end, NDBC54 (mean = 6.3 m/s) and the dominant wind direction at the east end is from the southwest whereas the west end had northwesterly winds. Also, the mean H_s was 0.9 m at the east end and 1.6 m at the west end. The September data also show a wider range of the IMF1 values at far ranges, about 30 to 40 km, than do the April 1999 data. The distribution histogram (Figure 5.8) reflects this since the 5 to 7 cm/s bin is now greater than the bin for 3 to 5 cm/s, the *reverse* of the situation for April 1999. The same spatial maps and scatter plots exist for August (not shown), a month with nearly the same mean H_s, 1.5 m, but much *greater* winds at the west end (mean = 10.1 m/s).

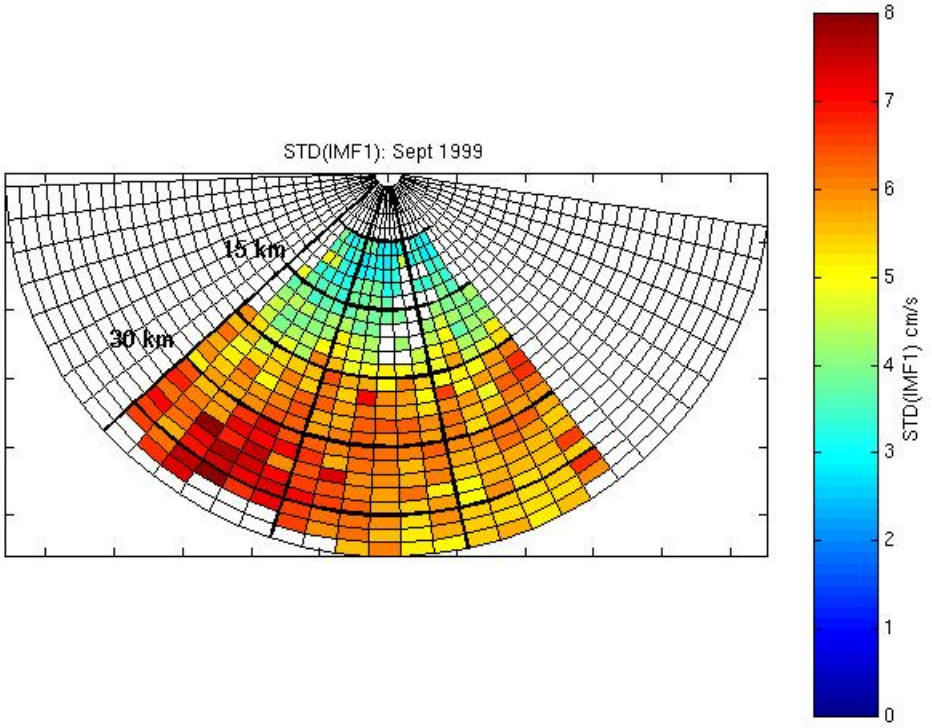

Figure 5.7 SBC: SI Spatial Distribution in Range/Azimuth for Sep 1999. White indicates missing.

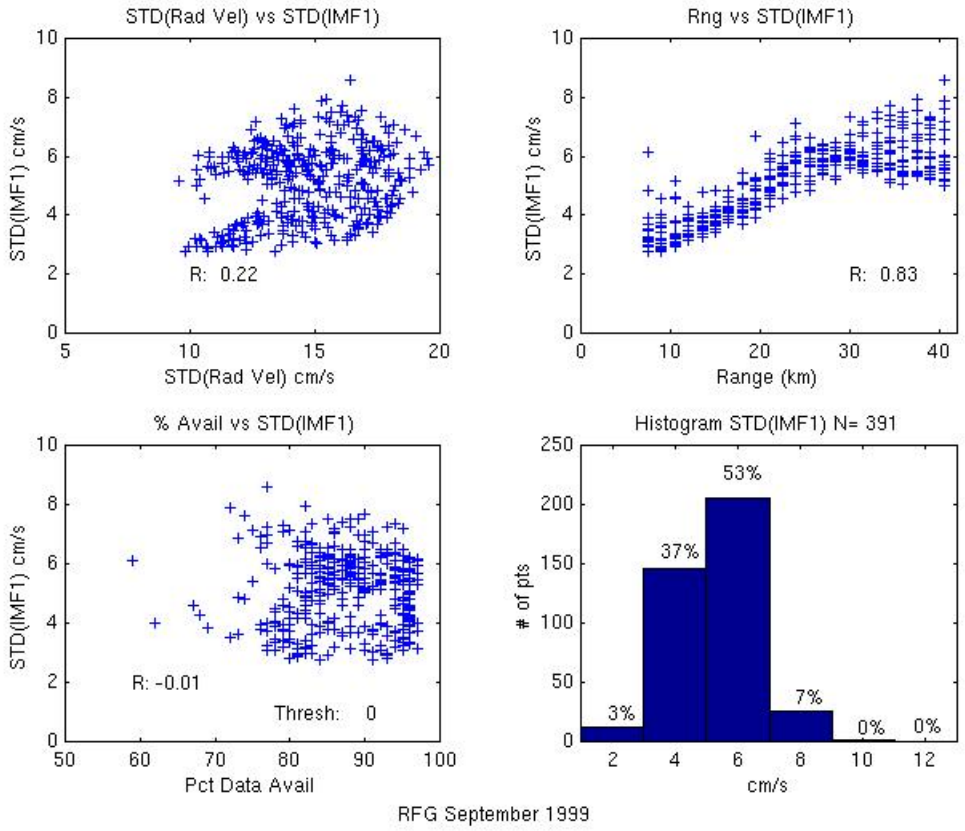

Figure 5.8 SBC: Sep 1999 SI vs RadVel (UL); SI vs Range (UR); SI vs %Cov (LL); Histogram SI (LR)

5.3.5 Results: St. Croix, U.S. Virgin Islands Data

Data from a radar that was identical to those deployed in California (except using a higher operating frequency) have also been examined, to determine whether the general features of IMF1 have a dependence on operating frequency. Part of the reasoning behind this is that the velocity resolution is improved (becomes smaller) by using higher radar frequencies, i.e. resolution = radar wavelength/coherent integration time. Coherent integration time was the same for both the St. Croix and California deployments. Therefore, the radar's velocity resolution is better at St. Croix. Specifically, for the St. Croix radar, the velocity resolution was ~2.3 cm/s, whereas, for the California radars, it was ~4.6 cm/s.

Briefly, the St. Croix radar's coverage area is characterized by deep water throughout but is protected by other islands from the direct effects of the Atlantic Ocean to the north. Therefore, wave action is small and is limited primarily to wind waves. During the radar deployment (Summer 1997), wave measurement data were not available. Wind speeds were relatively light, about 3 to 8 m/s. The details of this deployment and the associated data are presented in Harlan et al, 2002.

For the purposes of this report, times during the three-month deployment have been selected based on continuity of data. The scatter plots and histogram (Figure 5.9) resemble a combination of the California coastal site and the SBC site. There is no range dependence as for the open coastal site yet the histogram is similar to the SBC site, RFG, during April 1999 when the majority of the SI values are in the 3 to 5 cm/s bin. These data are suggestive of the lack of dependence of SI on radar operating frequency.

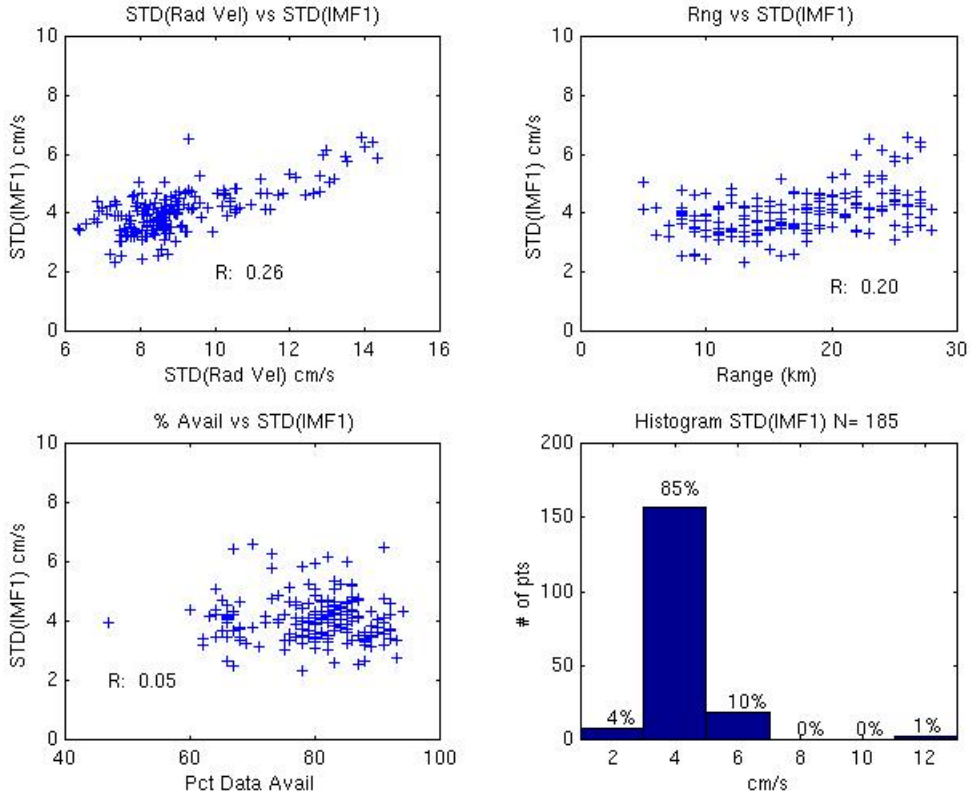

Figure 5.9 St Croix: Summer 1997 SI vs RadVel (UL); SI vs Range (UR); SI vs %Cov (LL); Histogram SI (LR)

5.4 Summary: Spatial Analysis Results

Addressing the questions posed above:

1. SI does not vary with the radial velocity. Therefore, it is a measurement that is derived from the complete time series but is not linearly related to it.
2. For open coastal sites, SI does not increase with range. However, for the SBC site RFG, there is a clear correlation of SI with range during both high and low wave regimes. Further, examining the data for August for RFG (not shown) shows the same patterns in both the scatter plots and the histogram as September despite the fact that the wind in August was considerably greater than that of September. This suggests that, for RFG, wind speed is not the dominant factor in determining the values of SI.
3. Filling in missing values does not increase SI, at least when the filling is no more than 20 percent of the total time series. (Until the percentage missing reaches about 40 to 50 percent, no relationship is found)
4. For the open coastal sites, SI values maintain a remarkably small range of values with nearly all values falling between 3 and 7 cm/s independent of wind or wave conditions. For the SBC site, SI values are largely between 3 and 5 cm/s during high wind/wave conditions of April.
5. Wind/wave conditions do not cause dramatic changes in IMF1 standard deviations at the open coastal site, FBK. For April, May, and September, the proportion of the 5 to 7 cm/s bin is greater than the 3 to 5 cm/s bin by a factor of 2 to 7, depending on month.
6. For the SBC site, the lighter wind/wave conditions actually result in greater values of SI with the largest proportion of SI shifting to 5 to 7 cm/s from 3 to 5 cm/s.
7. Data that were collected from a radar operating in St. Croix USVI at a radar frequency twice that of the California radars exhibit the same range of SI values as the California systems. Thus, radar operating frequency does not appear to influence the SI values. Furthermore, the St. Croix data do not show the spatial variability of the SBC systems, but are free from a spatial pattern as for the open coastal California radar. This is consistent with the fact that the St. Croix coverage region had no topographic or bathymetric features that might influence wave and current action. The actual distribution of SI values is toward lower values than those of the open coastal sites. This is consistent with the lack of wave action, as for the SBC site.

5.5 Additional Results from Spatial Analysis

5.5.1 Minimum SI Values

The nearshore ranges at RFG within the SBC consistently exhibit the smallest values of IMF1 standard deviations found throughout the time-space domain of this study. These values tend to be approximately 3 cm/s. *This suggests that this may be a minimum value found for hourly data over month-long time series since we assume*

that wave action is minimized in the SBC. The St. Croix data, having almost no wave action, also support this result.

5.5.2 Spectrum Power Spatial Distributions

To assess EMD with respect to conventional Fourier spectra of time series, the spectrum was computed for each range cell for the same month-long time series as used for the EMD. The original motivation for some of this work was the discrepancy seen in Fourier spectra of HF radar velocity as compared with nearby CM velocities. This discrepancy was most pronounced at frequencies above about 3 to 5 cpd where the CM spectra decreased rapidly while the HF spectra had a much flatter pattern.

After computing spectra for each radar cell, the power was integrated over frequencies from 3 cpd to 12 cpd (the Nyquist frequency). Spatial maps of this power reveal similar patterns to the SI spatial distribution (compare Figure 5.10 with Figure 5.1; compare Figure 5.11 with Figure 5.5; compare Figure 5.12 with Figure 5.3; compare Figure 5.13 with Figure 5.7), that is, no spatial pattern for the coastal site and a pattern of increasing power with range for the SBC site.

Although these spatial maps of power agree qualitatively with the spatial maps of SI, it should be kept in mind that the actual power values will vary with the window length and window type that are chosen for the Fourier Transform as well as the overlap chosen when using the Welch method for creating power spectra. Additionally, the values of SI are arguably a more intuitive measure of fluctuations in the data since SI is in cm/s, as are the current velocities themselves.

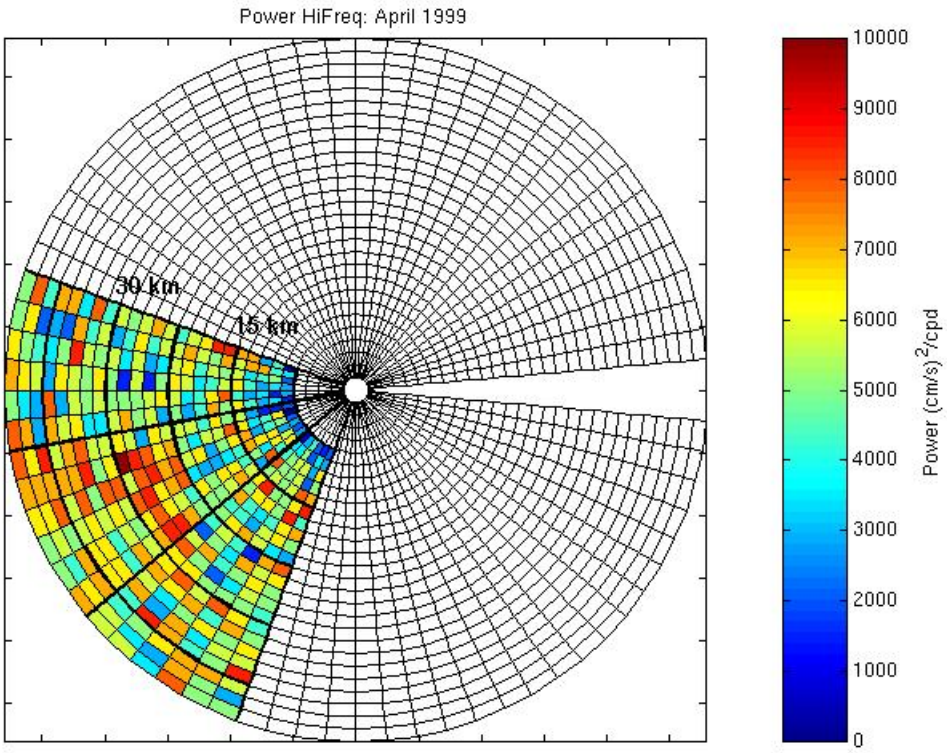

Figure 5.10 Coastal: Spectral Power Spatial Distribution for April 1999 $(cm/s)^2/cpd$

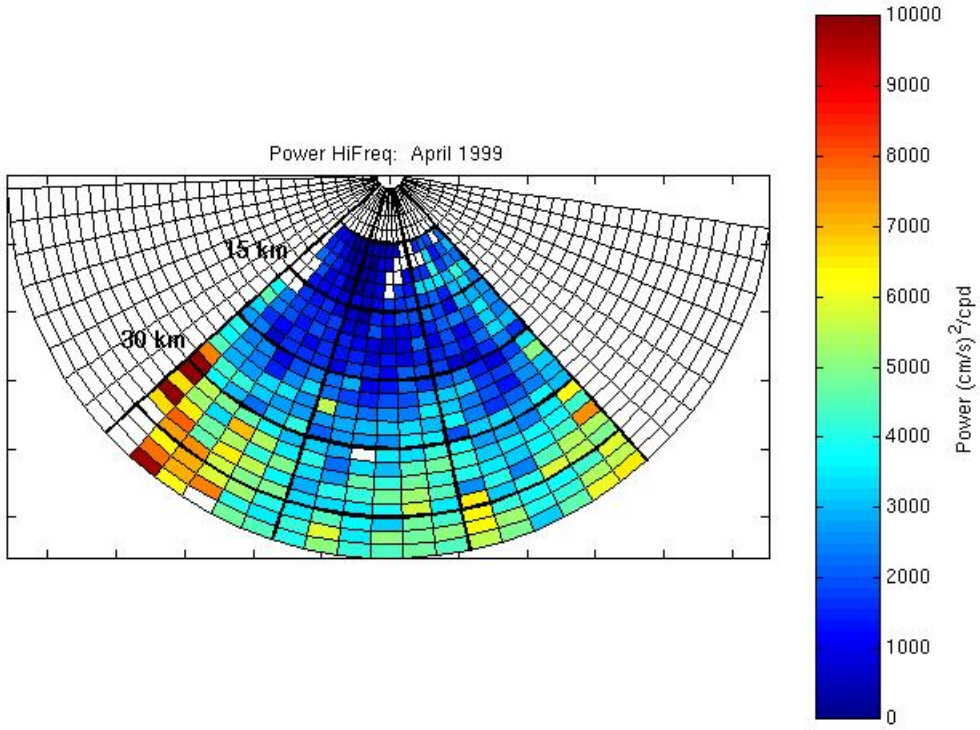

Figure 5.11 SBC: Spectral Power Spatial Distribution for April 1999 $(cm/s)^2/cpd$

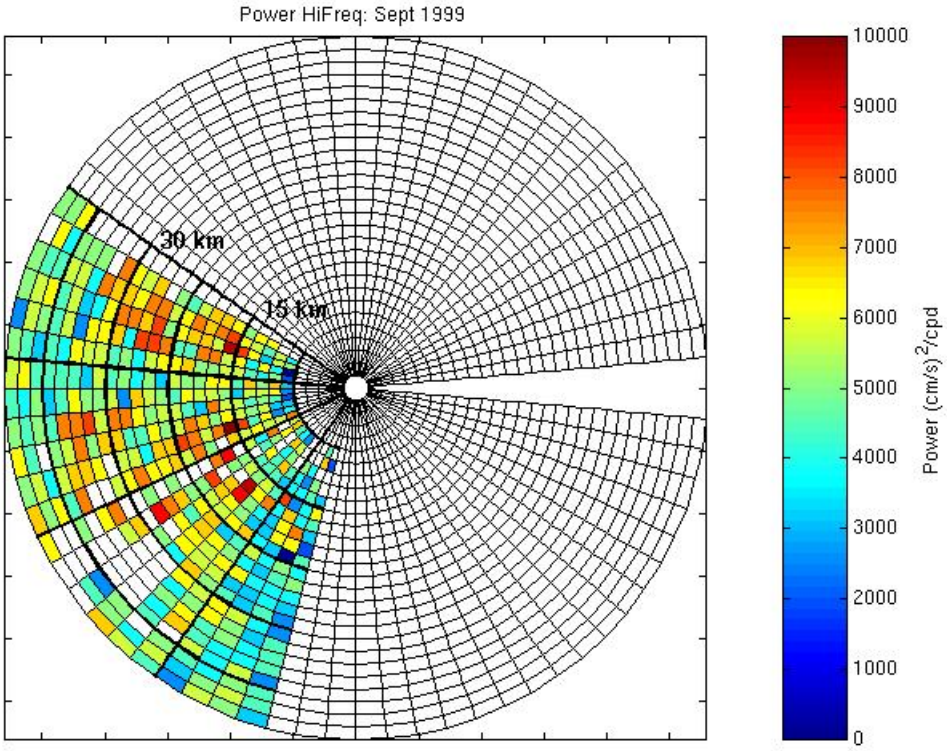

Figure 5.12 Coastal: Spectral Power Spatial Distribution for September 1999 $(cm/s)^2/cpd$

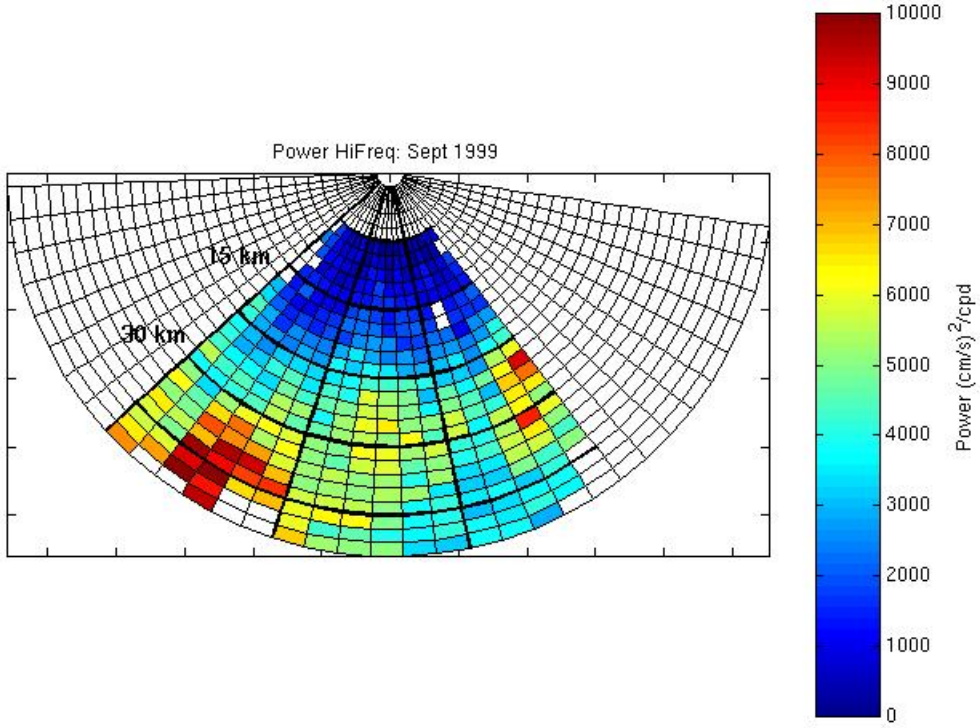

Figure 5.13 SBC: Spectral Power Spatial Distribution for September 1999 $(cm/s)^2/cpd$

6. Time Domain Analysis

Having discussed the characteristics of IMF1 for the coverage area of specific radars and for month-long time series, we now investigate temporal changes in IMF1. Several possible causes for large values of IMF1 will be explored. The causes can be broadly grouped as:

local wind-induced currents;
reductions in radar signal-to-noise ratio (SNR);
rapid changes in the sub-mesoscale current field;
wave-induced currents.

Each of these factors is to be studied separately below.

6.1 Methodology for IMF1 Time Domain Assessment

Empirical Mode Decomposition (EMD) is performed on each range-azimuth cell. Each azimuth nominally contains 28 usable range cells. For the FBK radar site, there are approximately 21 azimuths that have at least 75% complete temporal coverage for a given month. Therefore, there are potentially 588 individual time series for any chosen length of time. In this analysis, one-month time series of hourly data are used.

Initially, a subset of points within the 588 range-azimuth cells was chosen for use with EMD for comparison with nearby current meter data. Later, all range-azimuth cells were processed with EMD to allow for averaging of IMF1 across ranges.

For each time series of IMF1, the standard deviation of four-hour subsets of IMF1 (These standard deviations of IMF1 are henceforth referred to as simply “IMF1”) is computed. Four-hour subsets were chosen since the frequency at which the HF and CM power spectra diverge was approximately 3 to 5 cpd or 8 to 4.8 hour periods. A time series of these standard deviations of IMF1 are plotted as a function of range cell for a single azimuth. Three contiguous azimuths of the range-time-SI are shown in Figure 6.1.

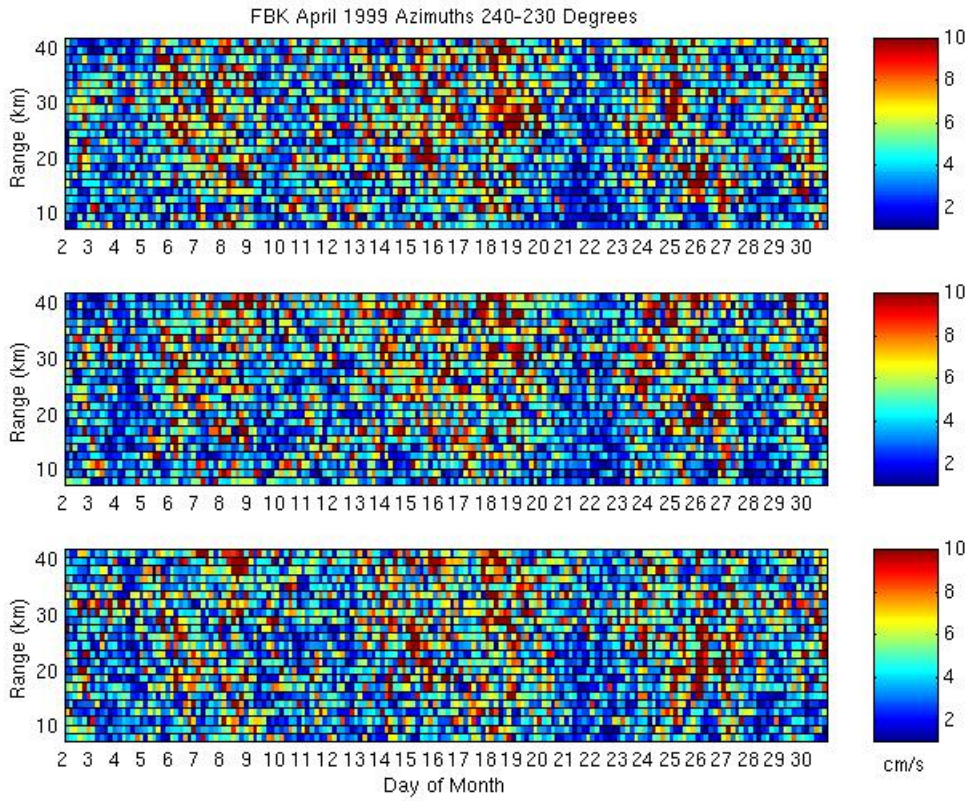

Figure 6.1 Example STD(IMF1)-Range-Time

Using these criteria, a wide range of wind, wave and surface current conditions are examined.

6.2 Analysis of Potential Causes for the Generation of Large IMF1 Values

In the following sections, several specific causes for the generation of the peak values in the IMF1 time series are investigated. Even though they were not found to be effective factors, these potential causes are included here for completeness.

6.2.1 Local Wind-Induced Currents

Wind-induced drift currents are typically estimated to be approximately 3% to 4% of the wind friction velocity or 1% of the wind speed at 10 m height, U_{10}. Short-time scale currents may result from sudden large wind increases. However, if the wind speed then becomes relatively constant, even at large speeds, it is expected that IMF1 peaks would not persist since IMF1 is limited to short time scale events. Whether this rapid increase in drift currents causes a peak in IMF1 values is examined here.

The wind speed time series at the NDBC buoy 46011 within the radar coverage area is compared with the IMF1 time series for the radar azimuths that are in the direction

of the dominant wind direction, i.e. northwest (Figure 6.2). To assess local wind-induced currents, azimuthal sectors that are nearest to the direction of the predominant wind are examined.

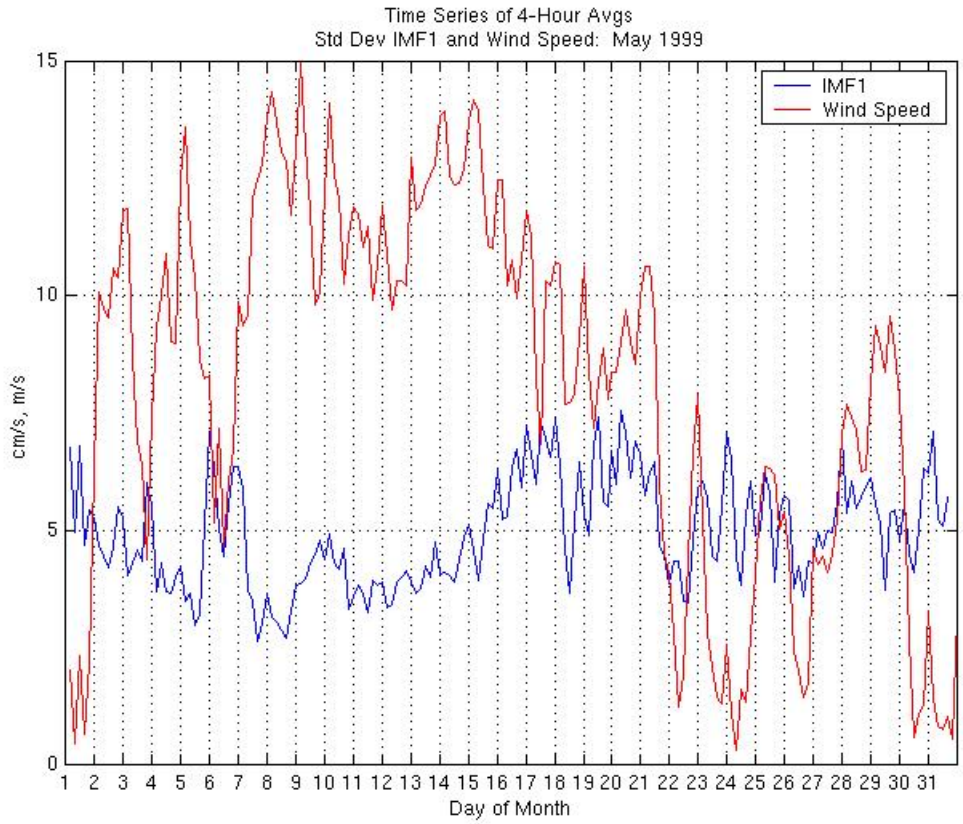

Figure 6.2 Wind Speed and STD(IMF1) May 1999

The correlation coefficient for the comparison of wind speed with IMF1 is -0.43 and -0.48 for April 1999 and May 1999, respectively. If large wind speeds were creating wind drift currents, then the correlation should be *positive* rather than negative as seen here. Thus, it is concluded that the wind-induced drift currents are not creating large fluctuations in IMF1.

6.2.2 Reductions in Radar SNR

The electromagnetic radar signal that backscatters from the sea surface is dependent on the presence of Bragg-resonant ocean waves. The algorithm that is used to compute the radial velocity from the Codar SeaSonde radar signal's Doppler velocity spectrum employs a form of Multiple Signal Classification or Multiple Signal Characterization (MUSIC) that is inherently dependent on the SNR. For the radars used in this study, the Bragg-resonant ocean waves have a wavelength of approximately 11 m. Clearly, the radar SNR is the most important determinant of accurate velocity retrievals and, in the limit of zero SNR, determines whether any information can be extracted from the Doppler velocity spectra.

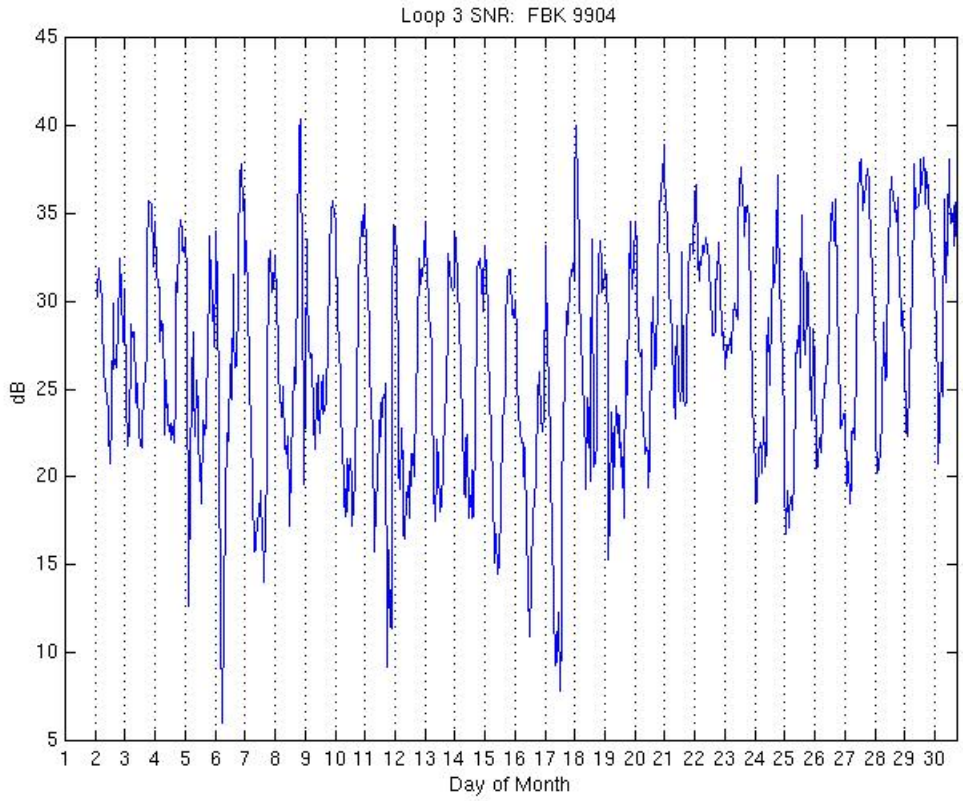

Figure 6.3 SNR April 1999

Other time periods (not shown) during May1999 exhibit about the same range of SNR values. For all the available time periods, the predominant feature of the SNR time series is the diurnal periodicity. This is a well-known feature of the HF electromagnetic spectrum which is due to the diurnal periodicity of the ionosphere. This ionospheric fluctuation allows the propagation over large distances of HF signals from other sources e.g. radio stations, lightning, at night, thus increasing the noise received by the radar and decreasing the SNR.

Another way of viewing the SNR, by proxy, is to examine the energy in the frequency spectrum of a wave buoy for the frequencies corresponding to the Bragg-resonant waves. Since these waves provide the "signal" for SNR, their absence should decrease SNR. Of course, this does not take into account any changes in the "noise" levels. Using the Harvest Platform directional wave buoy data and computing the integral of energy for a narrow frequency band (0.30 – 0.38 Hz), the time series of energy for Bragg-resonant waves for month of May1999 is shown (Figure 6.4).

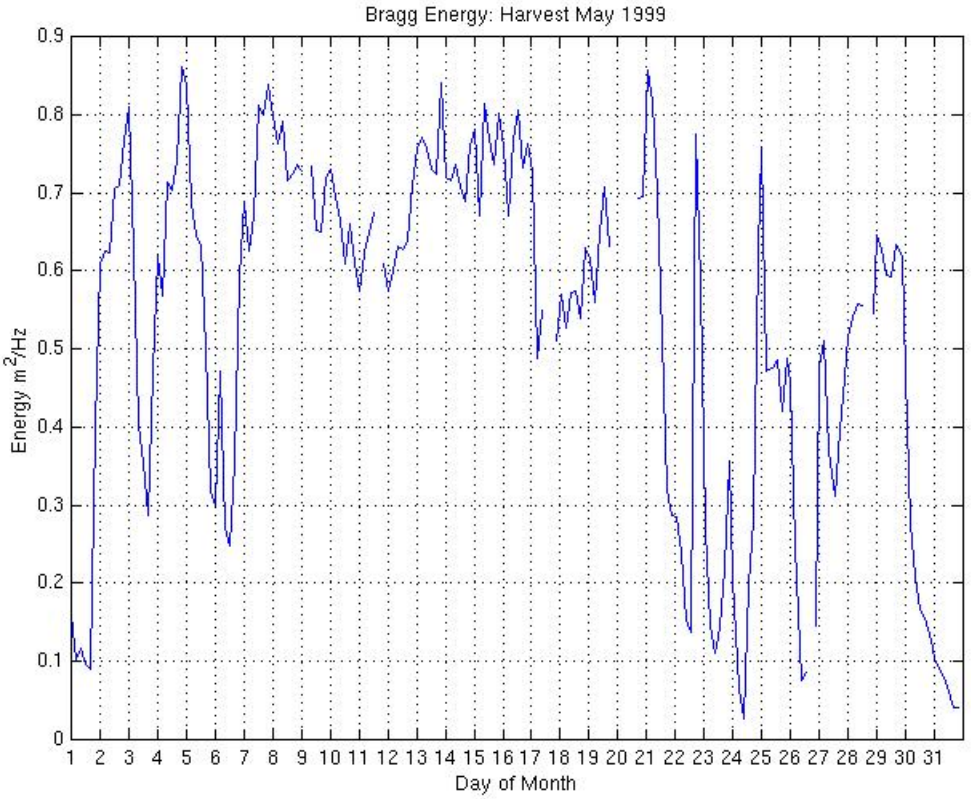

Figure 6.4 Energy of Bragg-Resonant Waves May 1999

Using one-hour averages, these energy levels also correlate strongly with the wind speed for each month (at zero hours lag) with correlations of 0.92, 0.92, 0.82 for April, May and September 1999, respectively. However, for the coastal site, FBK, it is clear that the energy of the Bragg-resonant waves is not, generally, related to the presence of IMF1 peaks (Figure 6.4). Thus, it is concluded that low SNR is not the cause of IMF1 peaks during these month-long time series for the coastal sites.

Within the SBC, the Refugio radar site (RFG) data exhibit a gradient of increasing IMF1 values from nearshore to the farthest radar points. This is exactly the *opposite* of the well-known wind speed gradient that occurs within the SBC, i.e., wind increases from nearshore to offshore. Therefore, if low wind speed is the primary cause of IMF1 values, the nearshore radar points should have greater IMF1 values than the offshore points since the wind speed is less near shore. The conclusion is that wind speed, and by proxy, SNR, is not the dominant mechanism for the gradient of IMF1 seen in the SBC.

6.2.3 Rapid Changes in Sub-Mesoscale Current Field

Sub-mesoscale processes include, for example, Langmuir circulation, small eddies, current fronts. The spatial resolution of the radar, as deployed during these time periods, is 1.5 km in range and varies from about 1 to 3 km in azimuth (e.g., at a mid-

range of 20 km, the azimuthal resolution is 1.74 km). Thus, Langmuir circulation effects would likely be masked within a typical radar cell. However, spatial changes in other sub-mesoscale currents due to fronts or eddies could be manifested as changes in radial velocities. It may safely be surmised that these sub-mesoscale processes would contribute to the velocity variability within a range cell. However, since there are no *in situ* measurements having small enough spatial resolution for intercomparison with the influence on the radar velocities of these small-spatial changes, these changes are not investigated here.

6.2.4 Wave-Induced Currents

Two wave phenomena that can produce wave-induced currents are: wave breaking and Stokes drift. To assess the maximum possible Stokes drift and wave breaking, it is reasonable to investigate the directions that are parallel to the predominant wave directions within a given time period. For the California coastal region under consideration, northwest is the primary direction of incident waves.

6.2.4.1 Wave Breaking

As mentioned previously, Banner et al., (2000) suggest a method for estimating the steepness of the local wind sea waves from the frequency spectrum of wave buoy measurements. Their *significant spectral peak steepness parameter, ε*, is a measure of both the nonlinearity of the local wind sea, as well as a measure of the steepness of the dominant waves of the local wind sea. Consequently, it has utility as a means of estimation of wave breaking which, in turn, generates surface currents. This spectral peak steepness parameter is defined as

$$\varepsilon = H_p k_p / 2$$

Where $H_p = 4\left[\int_{0.7 f_p}^{1.3 f_p} F(f)\,df\right]^{1/2}$

and $F(f)$ is the frequency spectrum and f_p is the peak frequency of the windsea. Values of ε more than a threshold value of about 0.05 to 0.06 were found to be associated with breaking wave events of the dominant wind sea waves. This particular parameterization of wave breaking is advantageous for use with the spatially distributed radar data since it characterizes the wave *field* rather than only an individual wave.

For May 1999, it is clear that the IMF1 events (Figure 6.5) are not associated with periods of large ε, the spectral peak steepness parameter. The correlation coefficient for this time period is -0.45. For further evidence of this lack of relationship, the correlation coefficient of IMF1 with ε for April 1999 was -0.25. As for wind speed, if wave breaking were an important process for IMF1, these correlations should be statistically significant and *positive*. Thus, it is concluded that wave breaking is not a significant factor in producing large IMF1 peaks.

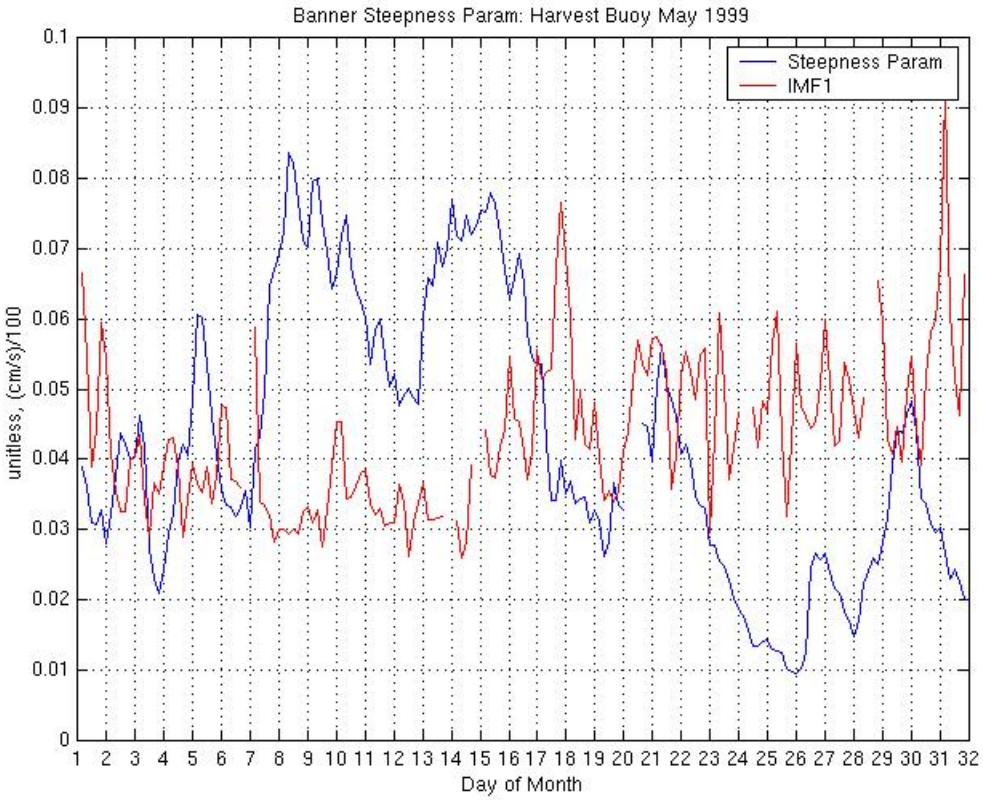

Figure 6.5 Banner Wave Breaking (Steepness) Parameter May 1999

6.2.4.2 Stokes Drift

A realistic surface wave, with finite amplitude, has a horizontal current velocity in the direction of propagation whose speed is given by the Stokes drift: $u_s = a^2 k \omega e^{-2kz}$, where a is the wave amplitude, k is the wavenumber, ω is the wave frequency and z is measured from the surface downward. At the ocean surface, the Stokes drift reduces to $u_s = a^2 k \omega$. Stokes drift can be estimated from the significant wave height, H_s, and wave period, T_p, information which are also given by a wave buoy. The wave frequency, ω, can be derived from the wave period as $\omega = 2\pi/T_p$. However, wavenumber is not measured directly, so it is derived from the linear dispersion relation. Of course, Stokes drift is dependent on *nonlinearity* of the wave, but this somewhat contradictory relationship must suffice in light of the available data. Additionally, to be rigorous, the wave amplitude should be used rather than H_s. However, this replacement for Stokes drift should only differ from Stokes drift by a small, although variable, amount and thus, its usefulness should apply to investigating the *relative* strength of Stokes drift events during a given time period.

As for wind-induced drift currents and wave breaking, a positive correlation between Stokes drift and IMF1 would serve as evidence of causation. However, for April and May 1999, the correlation coefficients are -0.25 and -0.14, respectively. Therefore, it

is concluded Stokes drift from the dominant wave direction is not a cause for large IMF1 peaks.

6.3 Alternative Cause: Wave Spectral Spreading and Stokes Drift

The previous analysis illustrates that no single one of the causes suggested above can account for the pattern of IMF1 peaks during a particular month. Cursory examination of wave directional spectral data from the Harvest buoy indicated that there may be a relationship between time periods of bimodal wave fields and times having large IMF1 peaks. In Figure 6.6, an example 30-minute-average wave directional spectrum for a period of large IMF1 values (April 16, 1999 0500 UTC) shows the two major components of the wave field propagating from the northwest and from the southwest.

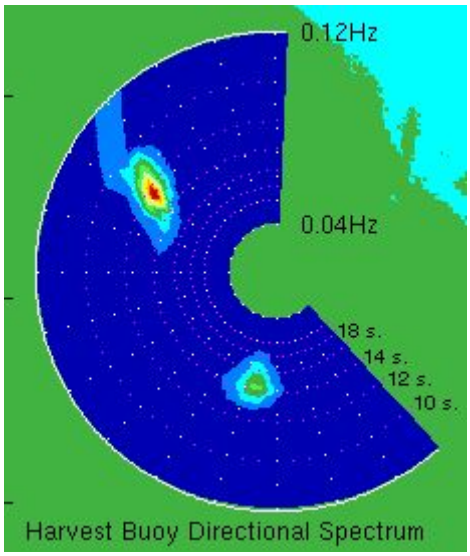

Figure 6.6 Harvest Directional Wave Spectrum for a Bimodal Wave Field: April 16, 1999 0500 UTC (courtesy UC-San Diego Scripps Institution of Oceanography Coastal Data Information Program)

Here it will be shown that the most compelling relationship for IMF1 peaks is that with *wave spectral spreading*.

6.3.1 Background

Here, time series of April and May 1999 and April 2000 are investigated for evidence of a relationship of IMF1 to wave spectral spreading events. It was found early in this research that the peaks of IMF1 are not linearly correlated to significant wave height as measured at the Harvest platform, i.e., standard correlation coefficients are not statistically significant. For example, for April 1999, the correlation is -0.14. Therefore, other wave spectra-derived parameters were investigated (Section 6.2). Bimodality of wave fields may be manifested in wave frequency or wave direction or both. There are a number of ways to parameterize bimodality of wave spectra in the frequency domain (see, for example, Massel, 1996; Ochi, 1998). Here, a similar method (Longuet-Higgins, 1983) is employed. The zeroth, first and second moments

of the frequency spectra are computed and the *frequency spread parameter* is $\nu^2 = (m_0 m_2 / m_1^2) - 1$. For a spectrum having a single frequency, $\nu \rightarrow 0$, and ν becomes larger for bimodal or multi-modal wave fields.

Representing the directional wave spectrum as a Fourier series:

$$S(\omega,\theta) = \tfrac{1}{2}a_0 + \sum a_n(\omega)\cos(n\theta) + b_n(\omega)\sin(n\theta)$$

For directional spreading, there are also several methods; although no single method has been universally accepted. The *directional rms spread function,* σ, (e.g., Walsh, 1985; Kuik et al., 1988) is computed as $\sigma^2 = 2\text{-}2r_1$ where r_1 is the fundamental of the first harmonic of the spreading function = $(a_1^2 + b_1^2)^{0.5} / a_0$ and a_n, b_n are the Fourier coefficients of the expansion of the directional wave spectrum.

The ocean wave regime within the Santa Barbara Channel is variable owing to complex nearshore bathymetry and the presence of the Channel Islands and Pt. Conception. These factors combine to cause a complex mix of refraction, diffraction and reflection of swell waves that propagate into the area from both northerly and southerly directions (O'Reilly et al., 2000).

If the IMF1 peaks are due to wave effects from multi-modal wave spectral distributions, in particular, then it would be expected that the radar data from within the SBC would not be strongly susceptible to those effects since the inner SBC is sheltered from south swell and somewhat sheltered from northwest swell. This sheltering effect and the complex wave action in the vicinity north of the Channel Islands (O'Reilly et al., 2000) lead the following discussions to focus on the coastal sites, rather than the SBC site.

6.3.2 Azimuthal Distribution of IMF1 Correlations

The correlation of IMF1 with spectral wave spreading parameters is investigated with respect to radar azimuthal direction. First, IMF1 is averaged over ranges 7.5 to 28 km for each azimuth. The averaged IMF1 value is then compared, via correlation, with each of the two wave spectral spreading parameters. The wave spreading parameters are only derived from a single buoy location, the Harvest buoy. The correlation is plotted with respect to azimuth. For April 1999, a pattern of increasing correlation in the vicinity of azimuth 225 to 265 degrees is present (Figure 6.7). The approximate value for which the correlation is significant is given as a straight line across each plot. The significance level is determined from the effective degrees of freedom for each time series of IMF1 (Emery and Thomson, 1997). Limiting the frequency spreading parameter computation to only those frequencies whose amplitude is at least 10% of the peak amplitude gives the green colored line. Although the statistical significance of this line is suspect, it indicates that azimuths in the vicinity of 230 degrees have the best correlation. This is supported by the May 1999 plot (Figure 6.8) which indicates that the best correlation is for azimuths 235 to 245.

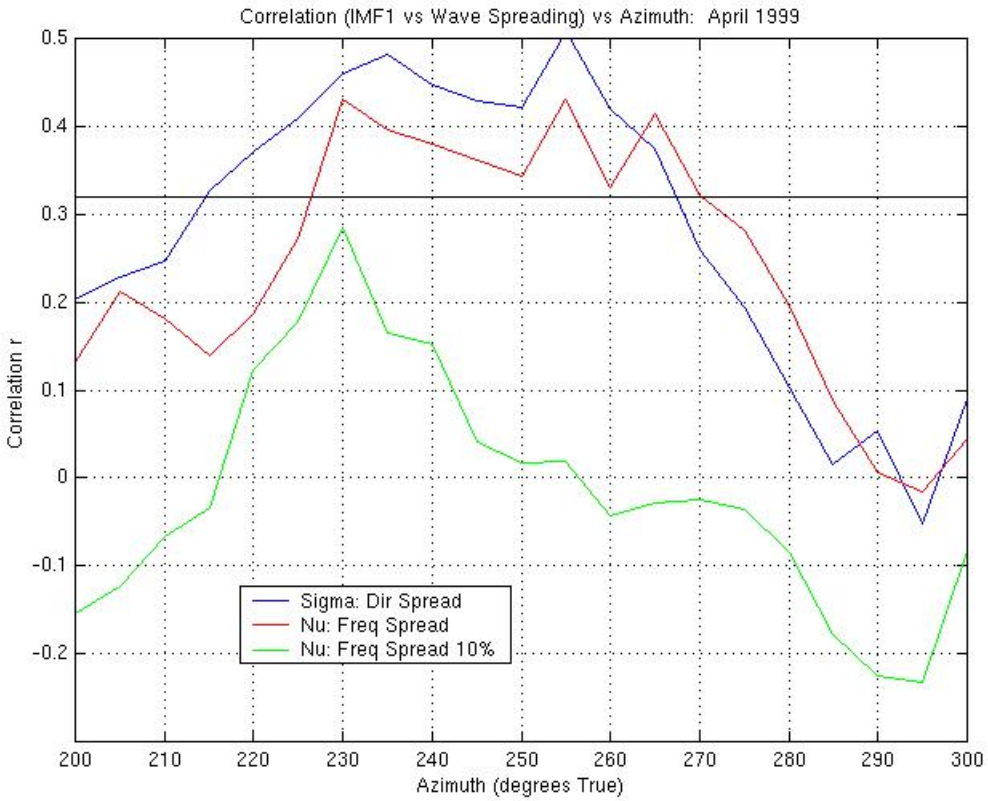

Figure 6.7 Correlation vs Azimuth April 1999

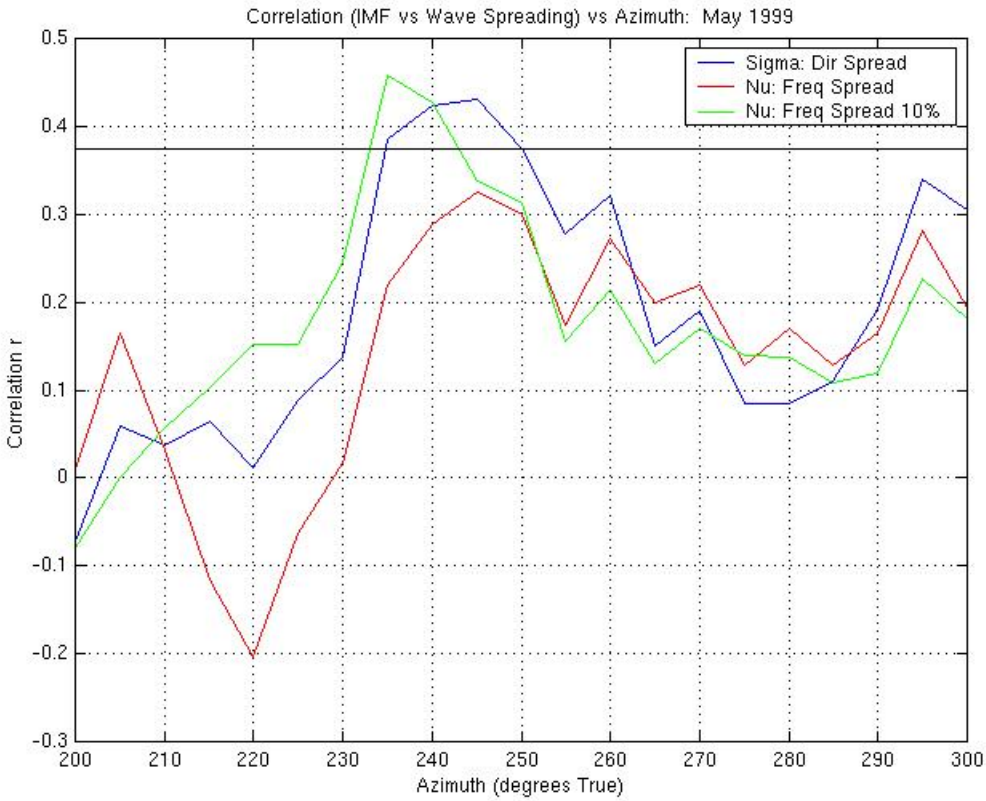

Figure 6.8 Correlation vs Azimuth May 1999

Similar plots are presented for April 2000, for the Pt. Arguello (ARG) radar location (Figure 6.9). In this case, the maximum correlation exists at azimuths of approximately 260 to 270 degrees.

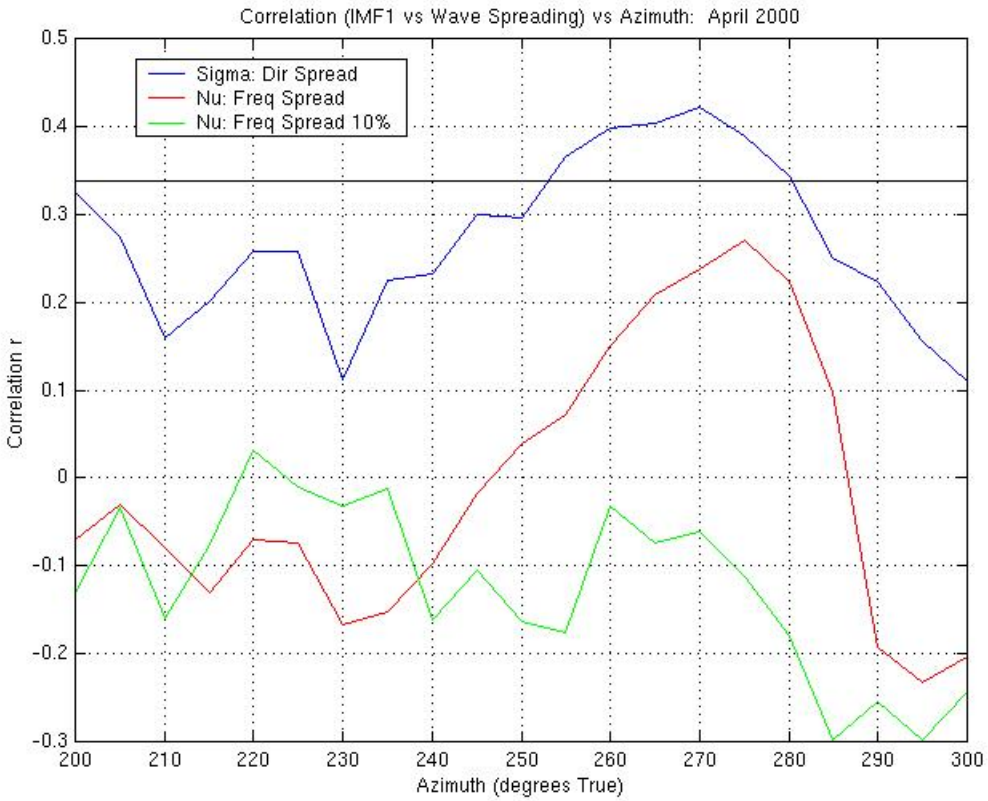

Figure 6.9 Correlation vs Azimuth April 2000

The geographic location of these azimuths nearly overlaps the location of the maximum correlations during 1999 from the Fallback 22 radar site (Figure 6.10).

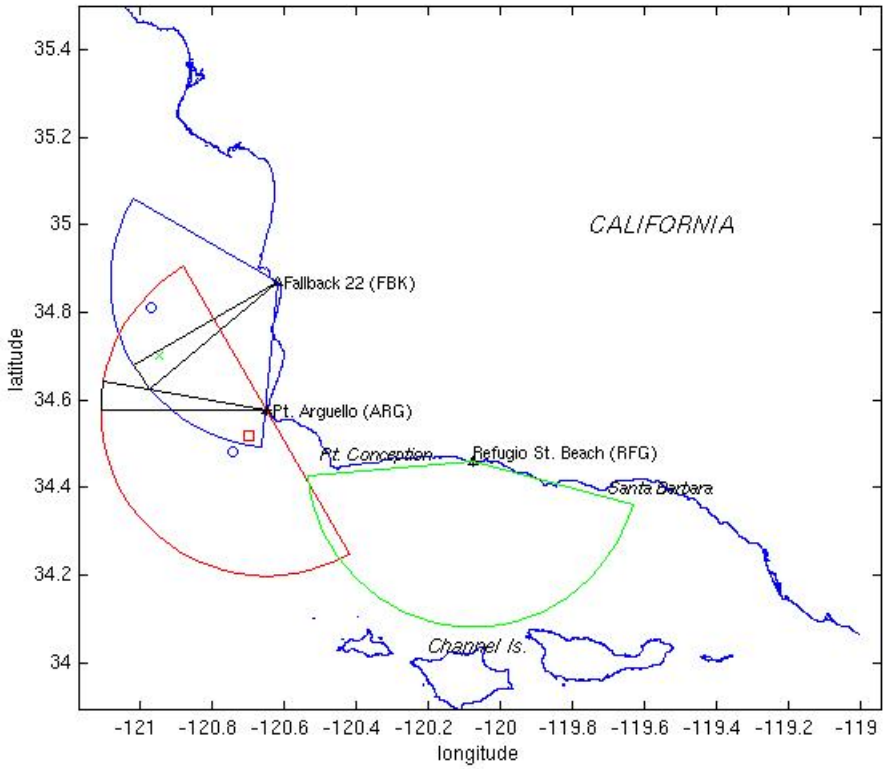

Figure 6.10 Map of Azimuths of Peak Correlation for 1999 and 2000

Sectors consisting of multiple azimuths, corresponding to the largest correlations in these plots, can then be chosen for comparison with other geophysical parameters. Using sectors of multiple azimuths also reduces the possibility of skewing the result by a single anomalous azimuth's IMF1 values.

6.3.3 April 1999: Large Waves, High Winds

Having a wide range of significant wave heights, current speeds and wind speeds, April 1999 presents an interesting case study. The wind, wave and surface current conditions for April 1999 can be summarized as follows: wind northwesterly at 7-17 m/s with lulls having southerly directions with speeds of 5 m/s or less (Figure 6.11); waves from the northwest with periods of bimodality combining southwesterly swell with the northwesterly swell and wind waves; significant wave heights of 2 to 6 m with a mean of 2.5 m; currents were southward with a mean speed of 24 (AROF) to 32 (SAOF) cm/s. Note that these discussions of April 1999 do not consider April 1 since there were no radar data available for that day.

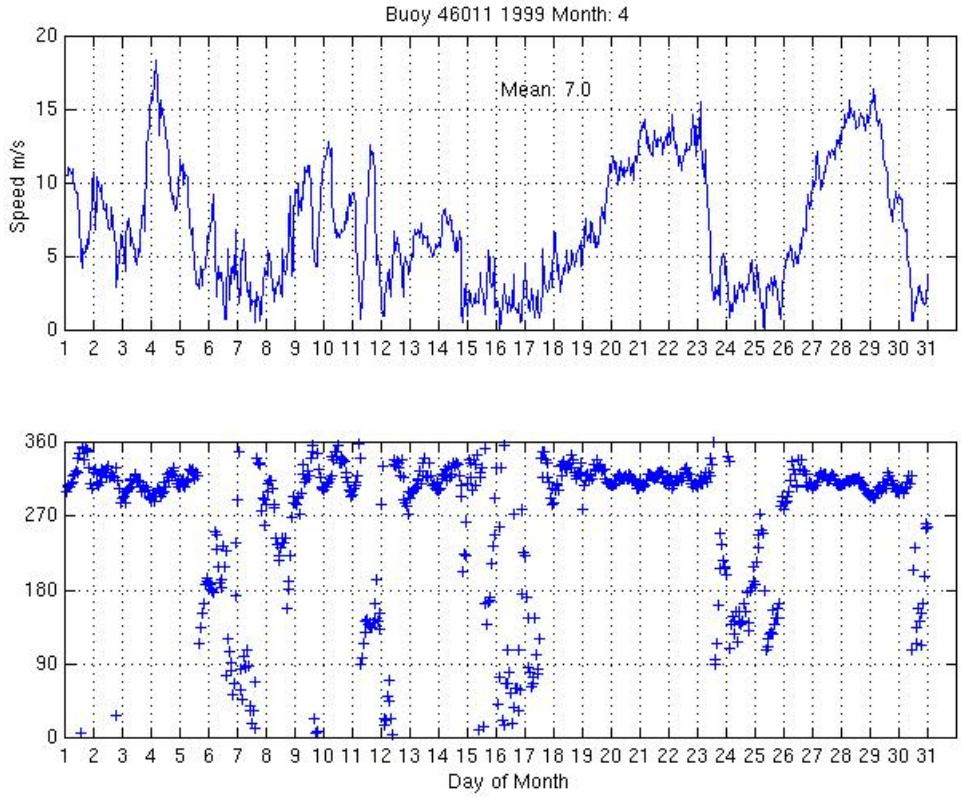

Figure 6.11 Wind Speed and Direction April 1999

Wave directional spectra from the Harvest platform are routinely computed and stored as half-hourly averages by the University of California-San Diego. These spectra were made available for the present study. Here, we averaged eight half-hourly spectra into 4-hour averages. The averaging was done in both wave frequency and direction.

The indication from the bidirectional fields discussed above is that the wave fields entering the radar coverage area during the times of large IMF1 peaks may be bimodal or multi-modal. Computing both of the spreading parameters from the Harvest platform data for April 1999 (Figure 6.12) illustrates that large values of each occur nearly simultaneously. The two parameters are correlated with a correlation, *r*, of 0.77. The peak wave direction of for each time period is also shown (Figure 6.12; top panel) to illustrate that bimodal spectra are often associated with southerly swell.

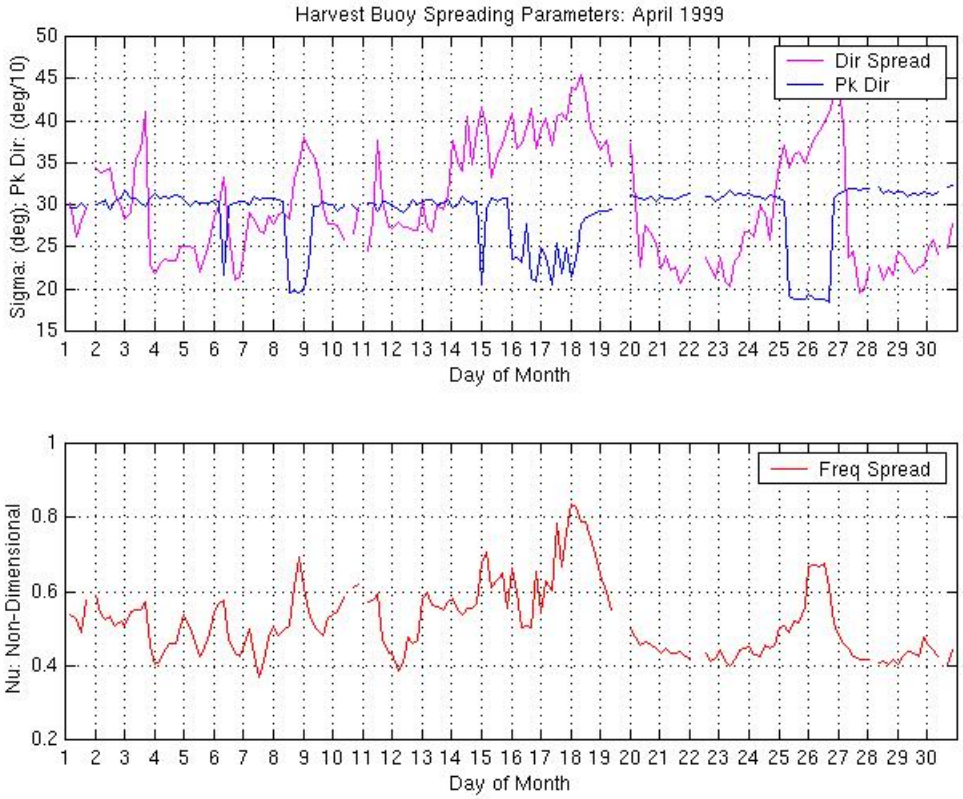

Figure 6.12 Wave Spreading Parameters April 1999

There are 174 values of each spreading parameter since they consist of 4-hour averages for the 696 hours from April 2-30. The conservatively chosen *effective degrees of freedom* (EDOF) were ~28 giving a 95% significance level of 0.36. Thus, for this time period, bimodal *frequency* spectra are typically accompanied by bimodal *directional* spectra.

The results of Section 6.3.2 suggest that radar azimuths centered on ~230 degrees True are appropriate for comparison.

A statistically significant negative correlation exists between wind speed and IMF1, i.e., large values of IMF1 are associated with low wind speeds ($r = -0.55$ with EDOF ~ 33). IMF1 was correlated with σ, the directional spreading parameter ($r = 0.52$ with EDOF ~30) and was also correlated with ν, the frequency spreading parameter ($r = 0.45$ with EDOF ~ 32)

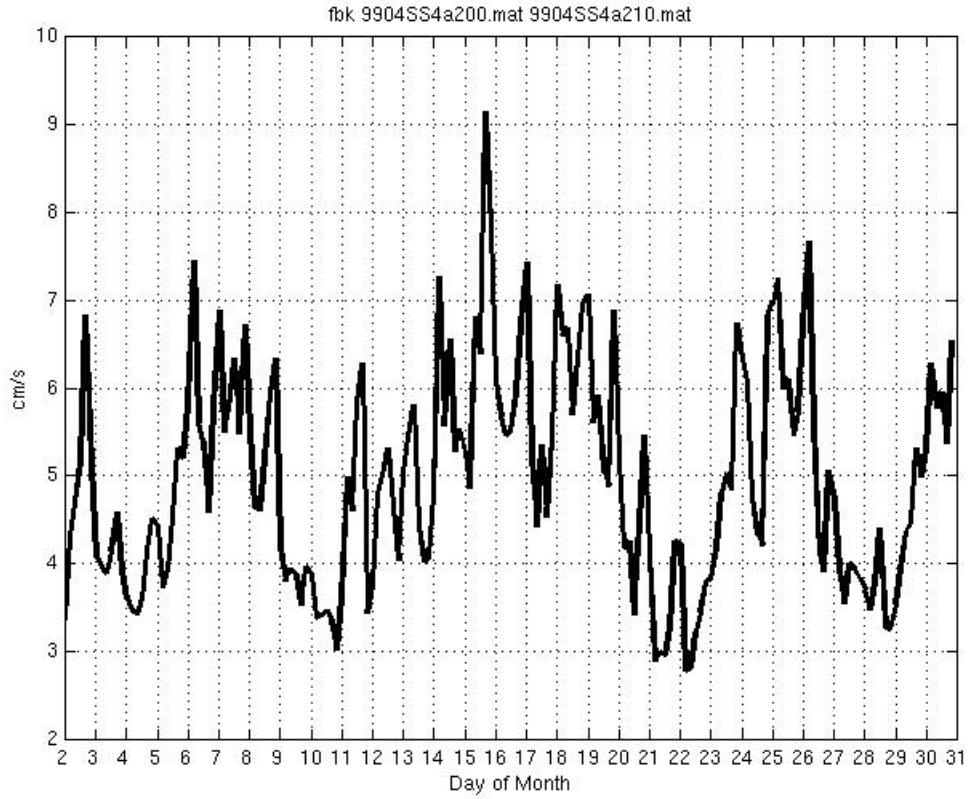

Figure 6.13 Mean STD(IMF1) Azimuths 240-250 Degrees T

Some specific examples of raw half-hour frequency and directional wave spectra are shown for time periods when IMF1 peaks are present and absent (Figure 6.14 and 6.15). In the unimodal example, Figure 6.15, it is notable that the energies for the southerly swell are less than one-tenth the value of the peak northwesterly energy values.

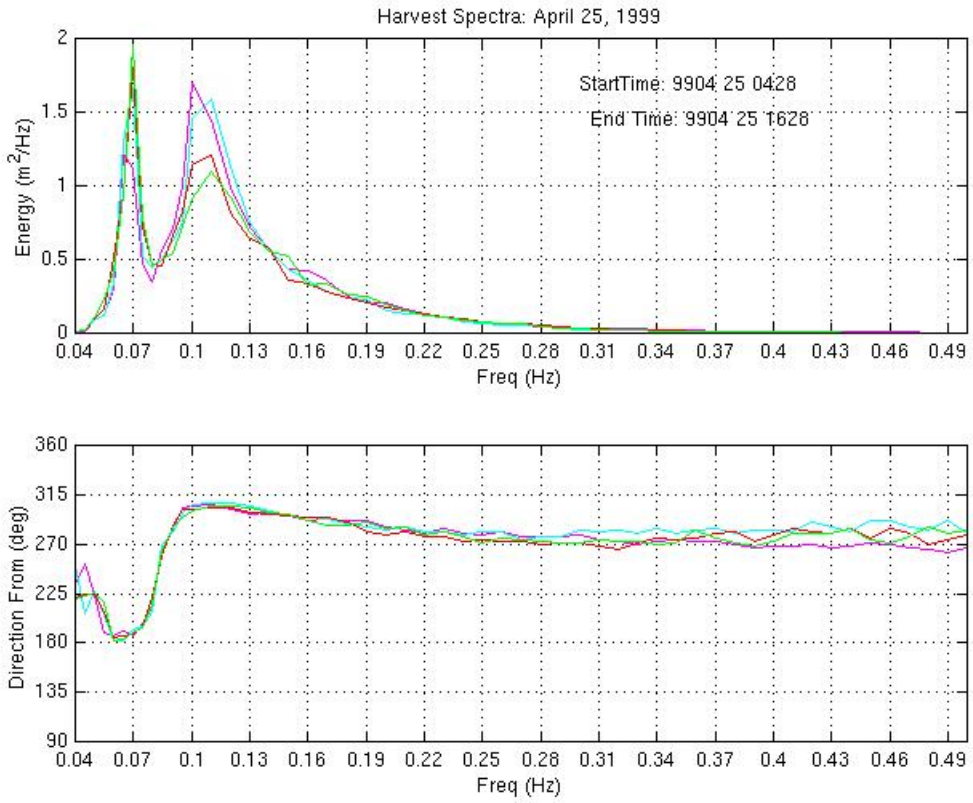

Figure 6.14 Example Bimodal Wave Spectra

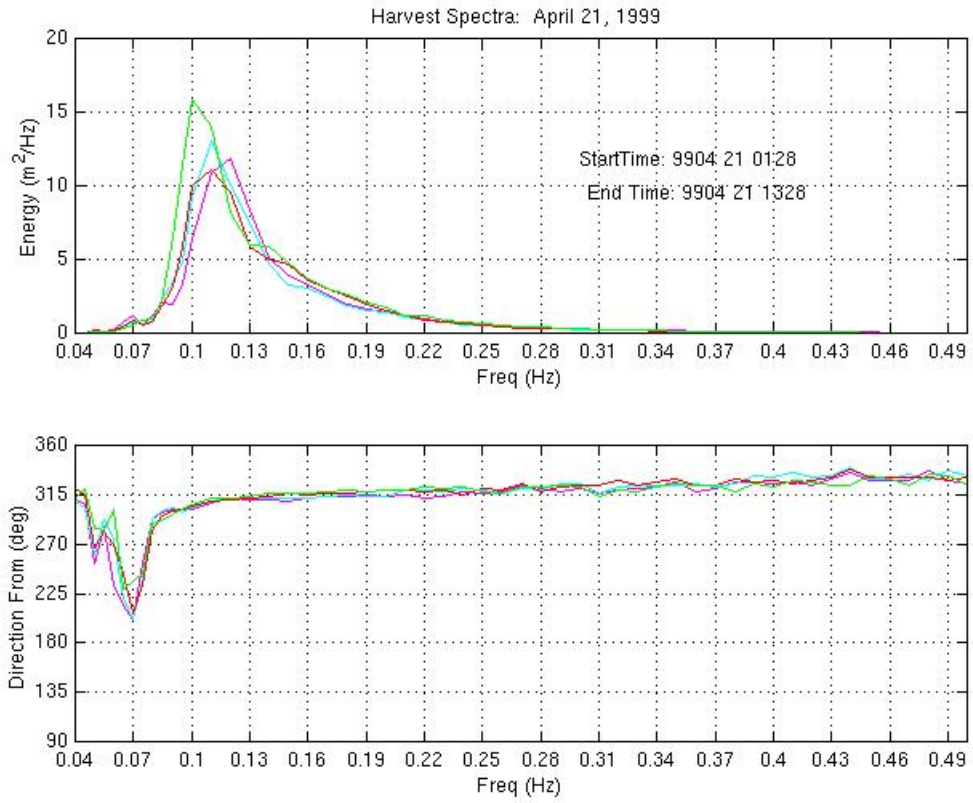

Figure 6.15 Example Unimodal Wave Spectra

6.3.4 May 1999: Large Waves, High Steady Winds

The wind, wave and surface current conditions for May 1999 are more complex than April 1999 and can be summarized as follows: wind consistently northwesterly at ~10 m/s for days 2 through 21 with lulls during days 1, 22-24, 26 and 30-31 with southerly directions and speeds of ~3 m/s or less (Figure 6.16); waves from the northwest with periods of bimodality combining southwesterly swell with the northwesterly swell and wind waves; currents were southward from day 1 through 17 with a mean speed of ~25 cm/s and then became highly variable during days 18-20, then shifted to northward for days 21 through 26 with speeds of ~13 cm/s for days 22-26, were generally southward for days 27 to 29 and then returned to northward during days 30 and 31. In the aggregate mean, these wind and wave conditions are similar to those of April 1999. The current speeds are generally lower than April but the directions are still predominantly southward.

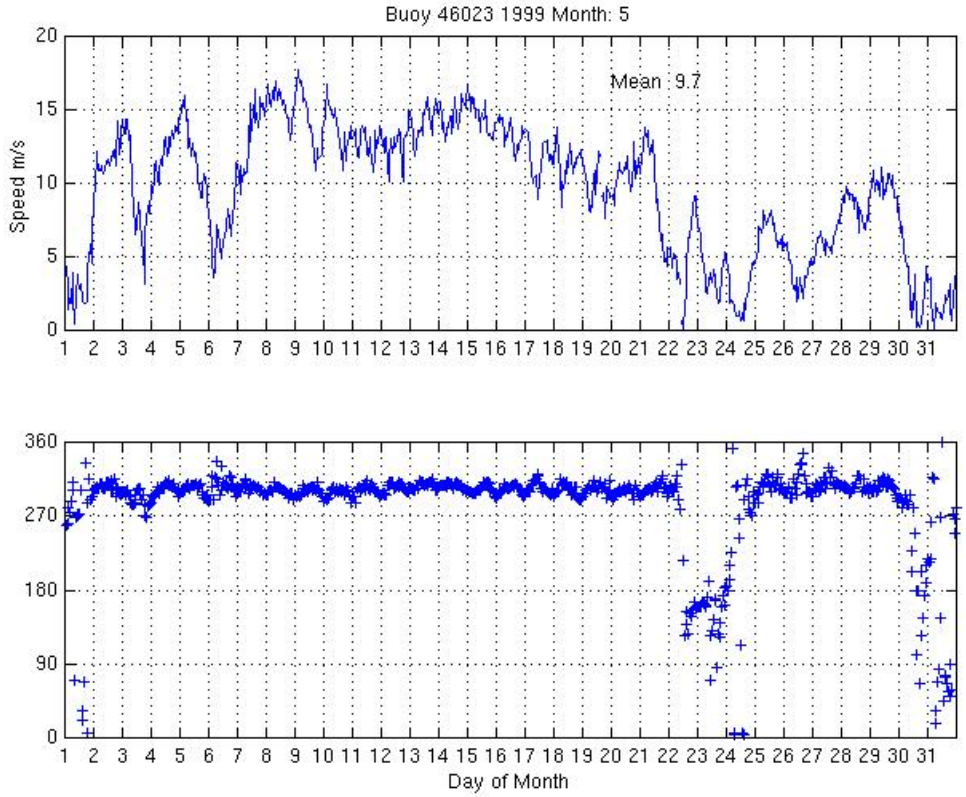

Figure 6.16 Wind Speed and Direction May 1999

The IMF1 peaks (Figure 6.17) tend to be shorter lived than for April 1999 but many peaks are evident.

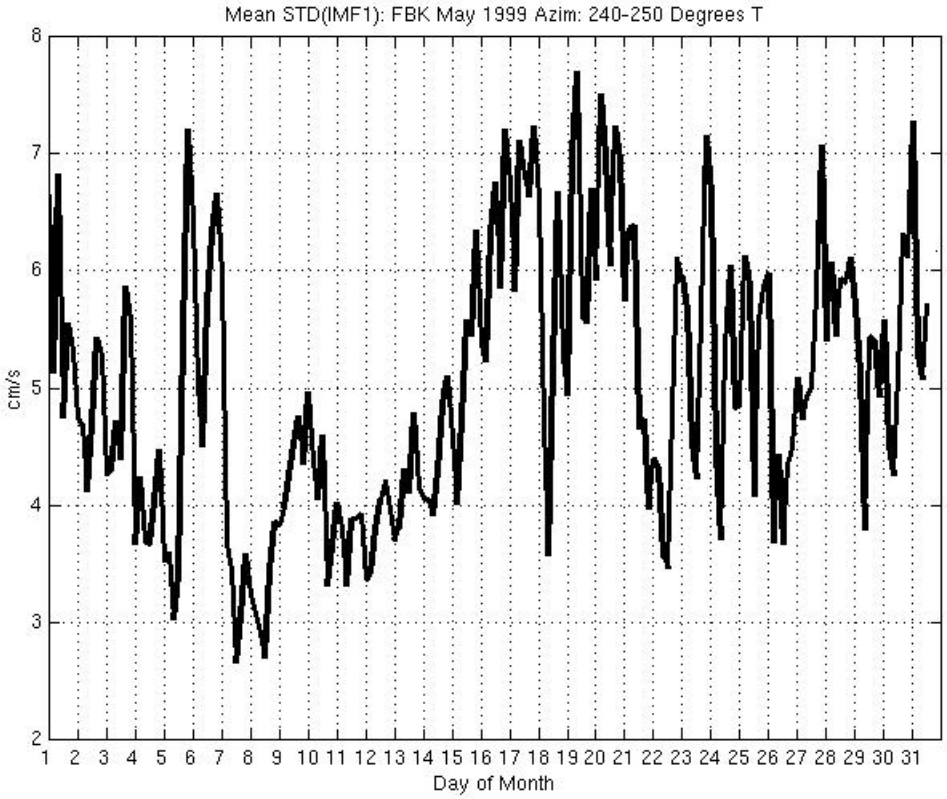

Figure 6.17 Mean STD(IMF1) May 1999 Azimuths 240-250 Degrees T

The spreading parameter plots illustrate periods of bimodality and a long period (May 8 through 15) of unimodality.

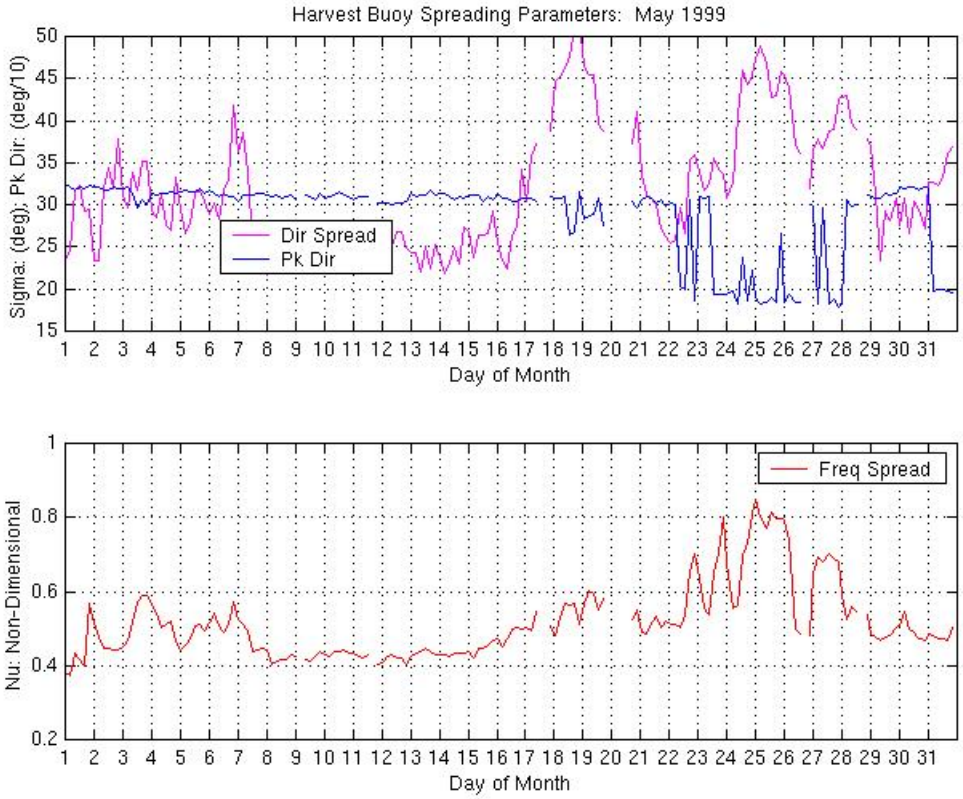

Figure 6.18 Wave Spreading Parameters May 1999

The wind speed was not correlated with IMF1 (r = -0.10). However, the directional spreading parameter, σ, was correlated at the 95% significance level (r = 0.45 with EDOF = 25) and the frequency spreading parameter, ν, was not well correlated at the 95% significance level (r = 0.34 with EDOF = 20). It should be noted that σ and ν are not as well correlated (r = 0.5) with one another for May 1999 compared with April 1999. However, computing ν using only swell waves gives r = 0.40 with EDOF = 34 which is significant at the 95% level and ν becomes more well correlated with σ (r = 0.6).

Since the correlations from April 1999 suggest that low wind speeds may be associated with IMF1 peaks, the consistent wind speeds and directions for May 2 to 21 permit further exploration of this relationship. Visual inspection of Figures 6.16 and 6.17 confirms the poor statistical relationship between wind speed and IMF1 shown above, i.e., the May 2 to 21 time period contains IMF1 peaks (May 6 to 7) as well as an extended IMF1 increase from days 18 to 20. These peaks are coincident with peaks in the directional spreading parameter, σ.

Here, a number of specific times during May 1999 are chosen for comparison of wave frequency-direction spectra with IMF1 peaks. This allows for detailed examination of the temporal changes in IMF1 and their relation to the spreading

parameters and to the wind (Figures 6.16, 6.17, 6.18). Also, it illustrates how the spreading parameter algorithms sometimes fail to coincide with large values of IMF1. At times, this is due to the lack of sophistication of the algorithm and at other times, it is due to real processes, e.g. a large wind event, that triggers a large IMF1 value in the absence of wave spreading.

Day 1: At the end of the day, there is a rapid increase in wind speed that coincides with a peak in IMF1 and a peak in the frequency spreading parameter, ν, but not the directional spreading parameter, σ, which exemplifies the lower monthly correlation between ν and σ. This also is an example of how wind can create a surface current, manifested by the IMF1 peak. The frequency spectrum (not shown) has an additional peak at higher frequencies (~0.25 Hz) which is reflected in the peak in ν.

Days 18 to 20: Both wind speed and direction are relatively constant with speeds of ~7 to 11 m/s and directions varying only ~20 degrees. The directional and frequency spreading parameters both experience a gradual increase then decrease by the 21st. The IMF1 peaks also exhibit the same general behavior. This example also suggests wave spreading processes are important.

Day 23: A distinct IMF1 peak late on this day is associated with a wind speed lull and wind direction shift and with a peak in frequency spreading parameter.

Days 25 and 28: Large IMF1 peaks, as well as peaks in both spreading parameters, but without a wind speed lull suggest a relation between IMF1 and the wave field, rather than between wind speed and IMF1.

6.3.5 April 2000: Large Waves, High Winds

Lacking data from the Fallback 22 radar site during 2000, the coastal site, Pt. Arguello (ARG), is used. The wind conditions for April 2000 were similar to April 1999 (Figure 6.19). The wave field exhibited a mean significant wave height of 2.2 m. Currents were southward with a mean speed of 25 cm/s. The correlations of the wave spreading parameters with IMF1 are: 0.43 for σ (significant at the 95% level), and 0.26 for ν (not significant). As for April 1999 and May 1999, the directional spreading parameter has better correlation with IMF1 than the frequency spreading parameter.

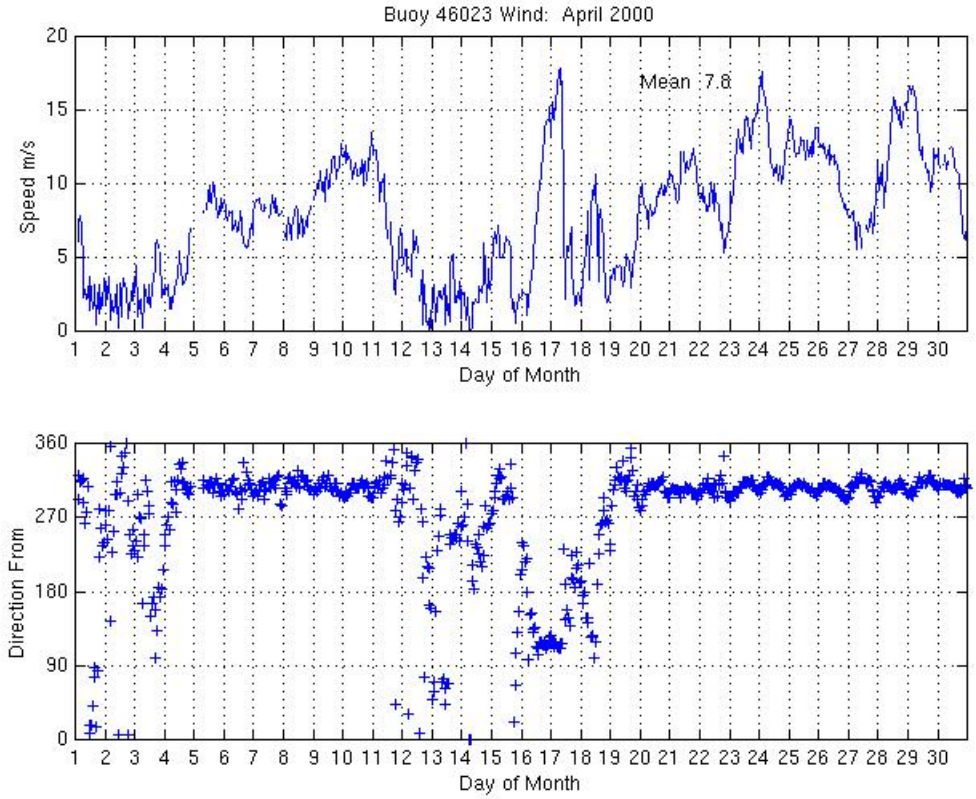

Figure 6.19 Wind Speed and Direction April 2000

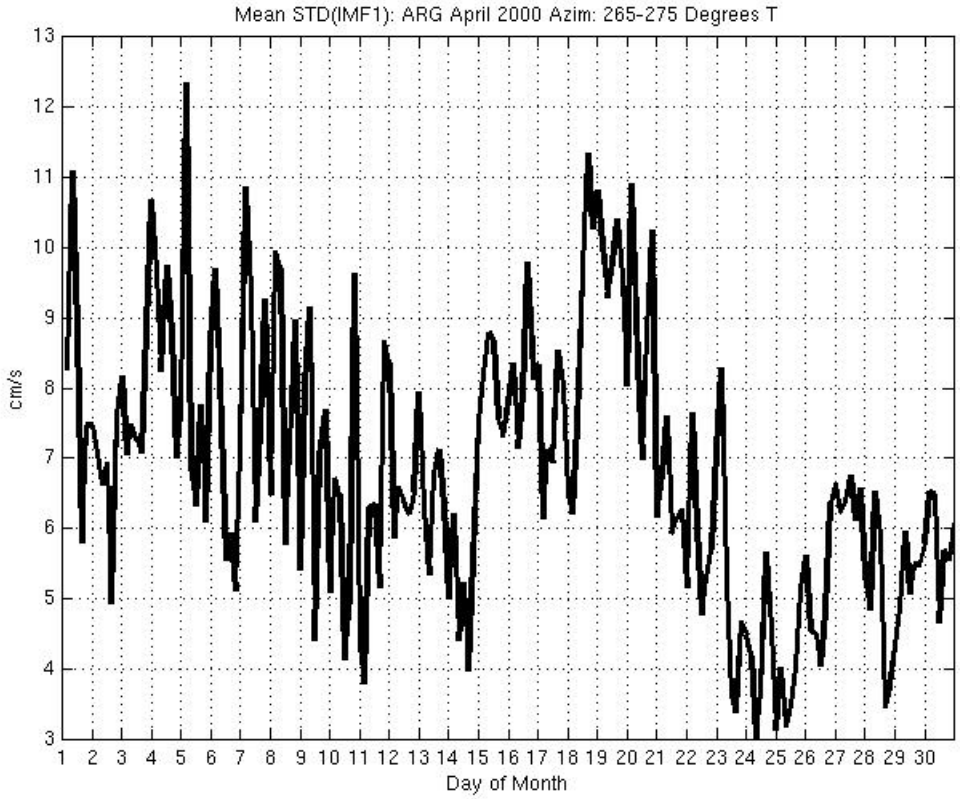

Figure 6.20 Mean STD(IMF1) April 2000 Azimuths 175-185 Degrees T

6.3.6 Pseudo-Stokes Drift from Bimodal Wave Directional Spectra

Values of the standard deviation of IMF1 that are approximately 3 to 5 cm/s would be large enough to create a peak in the IMF1 time series. Therefore, an estimate for the necessary wave parameters that would produce a 3 to 5 cm/s velocity is explored.

Stokes Velocity	Wave Frequency	Wave Amplitude
0.03 m/s	0.08 Hz	1.6 m
0.03	0.065	2.1
0.05	0.08	2.0
0.05	0.065	2.7

Table II Hypothetical Wave Frequency & Amplitude Necessary for Given Stokes Velocity

These wave amplitudes (Table II) are reasonable for the California coastal region under consideration. For example, during April and May 1999, the mean significant wave heights were 2.5 m and 2.4 m, respectively. Wave amplitude is generally considered to be one-half the wave height, so the mean significant wave heights

would translate to 1.25 m and 1.2 m wave amplitudes for April and May 1999, respectively. These values are slightly lower than the 1.6 m wave amplitude necessary to produce a 0.03 m/s Stokes velocity. Approached differently, the Stokes drift that would result from a 1.25 m wave amplitude and a 0.08 Hz wave frequency is 0.02 m/s. These estimates are close to the necessary values for producing the IMF1 peaks. It should be noted that the estimates for wavenumber used here are based upon the linear dispersion relation which is contradictory since the Stokes drift is a nonlinear wave phenomenon. However, no estimates from actual data are available. Approached a third way, to determine what wave frequency would be necessary to produce a 0.03 cm/s Stokes drift when given a 1.25 m wave amplitude, a wave frequency and period of 0.09 Hz and 11 s, respectively, is obtained.

Given an example bimodal wave directional spectrum, the procedure for estimating a pseudo-stokes drift is described. The spectrum is partitioned into two sections such that each section comprises a separate direction of the wave field. Using the direction vs. frequency plot as a guide, the two partitions are identified with respect to frequency (Figure 6.21, top panel). Then, as in Section 6.2.4.b, pseudo-Stokes drift is $u_s = a^2 k\omega$, where a, the wave amplitude, is estimated for each partition. The power (units: m^2/Hz) under the spectrum within each partition is summed. To provide an estimate for the wave amplitude, the summed power is then multiplied by the mean frequency of the partition and the square root is taken giving a value in units of meters.

It is found that the estimate of pseudo-Stokes drift for each partition are of the same order of magnitude and that their ratio is $O(1)$. In the example (Figure 6.21), the wave partition from the southwest has a mean frequency of ~0.07 while the northwest partition has a mean frequency of 0.10 and the ratio of the two pseudo-Stokes drift values is 0.68.

Similar bimodal spectra provide the same $O(1)$ ratios (not shown). And, as expected, spectra that are unimodal exhibit ratios that are $>> O(1)$.

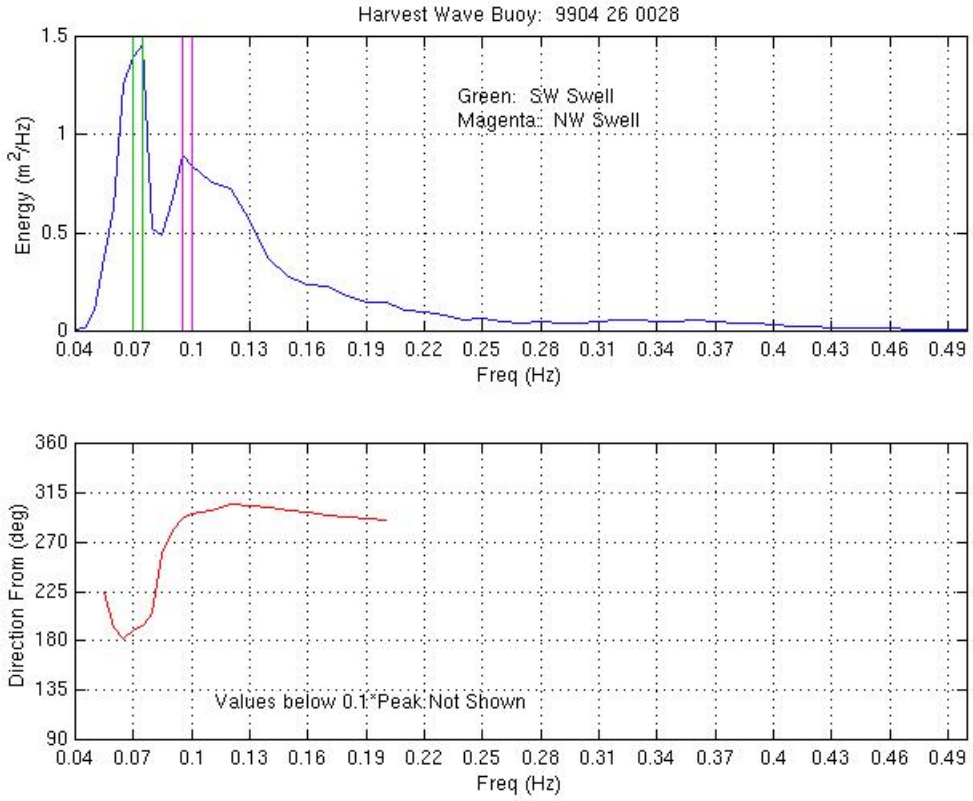

Figure 6.21 Example of Bimodal Spectra and Pseudo-Stokes Computation

7. Conclusions

Empirical Mode Decomposition has been applied to time series of HF-radar-derived radial current velocities and CM radial current velocities to investigate the short time scale motions of HF-radar-derived velocities. The decomposition produces an intrinsic mode function that is associated with the shortest time scale motions, denoted "IMF1".

7.1 Conclusions from Colocated CM and HF Data

Analysis of IMF1 for both CM time series and nearby HF-derived time series produced the following conclusions:

- IMF1 from HF time series contain no tidal motions, i.e. IMF1 is entirely super-tidal for HF time series. Huang et al. (1998), in creating EMD, asserted that each IMF contains motions that are inherent to some physical time scale. This result supports that assertion.

- Removing IMF1 from HF time series leads to spectra that contain less energy at frequencies greater than 3 to 5 cpd than do the coincident spectra for the complete time series of a CM. This suggests that some of the motions measured by HF at these super-tidal frequencies are physical processes, not simply "noise" in the HF measurement.

- IMF1 from CM time series may contain tidal motions. This is an example of a case when IMF1 is "mixed mode", i.e., contains motions from two or more physical processes, as discussed in Huang et al. (1998). However, by using IMF1 as a guide to selecting portions of the time series not having mixed modes, removal of IMF1 does not change the energy in the tidal band spectra. This agrees with the result, above, that HF IMF1 is super-tidal.

7.2 Conclusions from Analysis of Spatial Distribution of SI

Standard deviations of month-long time series of IMF1 (SI) obtained from HF time series were computed at each point within a radar's coverage area. The most significant conclusions from the analysis of the spatial distribution of the standard deviation of IMF1 from HF time series were:

- SI spans a relatively small spread of values: about 3 to 7 cm/s.

- The open coastal site exhibits no trends in SI with range, azimuth or with season, i.e., wind speeds and wave heights.

- The SBC site shows a trend of increasing SI with range, independent of wind or waves. If this trend were due to a trend in the wind, it should be in the opposite direction i.e., the SI should be larger near shore, in order to agree

with the findings from the time domain analysis portion of this thesis. Since this is not the case, the trend is clearly not due to a wind effect, but may be due to a wave effect. The specific nature of the effect cannot be determined at this time because of lack of wave directional spectrum data throughout the region where the trend occurs. However, results of swell wave modeling by O'Reilly et al. (2000) suggest that the wave field in this region is comprised of complex interactions of wave fields due to reflection, refraction and diffraction.

- SI also appears to be independent of radar operational frequency. This is based on HF radars operating at ~13 MHz and 25 MHz. The range of values for SI was the same for both radar frequencies.

- SI approaches a minimum value of ~3 cm/s within the SBC and at the island of St. Croix which suggests that the absence of wave action allows for this minimum to be reached.

- Integrated power for HF-derived spectra at frequencies greater than 3 cpd exhibits the same spatial characteristics as the SI plots: no trends with range or azimuth for the coastal site and a trend of increasing power with range for the SBC site. This indicates that SI and conventional periodogram-derived spectra are each measuring similar motions.

7.3 Conclusions from Analysis of IMF1 Time Series and Geophysical Parameters

The standard deviation of IMF1 (SI) was computed for 4-hour subsets within a month-long time series. These values were then compared with a number of geophysical parameters to determine correlations. Initially, it was hypothesized that current-inducing processes such as wave breaking, wind speed and nonlinear wave-wave interaction might be among the causes of the high frequency flattening of HF radar-derived velocity power spectra. It was found that wave breaking and wind-drift currents were not well correlated with SI. Some findings were:

Although low wind speeds appear to be correlated with SI for April 1999, it was found that SI during that time was also correlated with the bimodality or spreading of the wave spectrum. The bimodality was measured as a function of both the wave frequency spectrum and the wave direction spectrum. The correlation of wave bimodality and SI was corroborated by the May 1999 data, but the wind speed was not correlated with SI. Data from a different radar system from April 2000 also supports the correlation of SI with wave bimodality. It is concluded that wave processes are more important than wind-induced currents. The azimuthal distributions of these correlations from the two radar sites overlap suggesting that some wave process(es) act in a synergetic manner at that particular location of the ocean surface. Additionally, it was found that the correlation of SI with the wave directional spreading parameter, σ, was greater than the correlation of SI with the

wave frequency spreading parameter, ν. This also lends credence to the idea of wave-induced currents from two directions causing an increase in SI.

A pseudo-Stokes drift was computed from each directional peak in the wave spectra during times of bimodality. During these times, it was found that the two pseudo-Stokes drift currents were of the same approximate size; i.e., their ratio was $O(1)$. These nearly-orthogonal drift currents would add to the complexity of the local current field which in turn would both be contained in the radar Doppler spectra. This added complexity would present a more difficult task for a HF radar signal processing algorithm that extracts current velocity information from the Doppler spectra. Consequently, the geophysical process of wave bimodality appears to be related to increases in the short time scale motions in HF radar velocity measurements.

The proposed process of bimodal wave field-induced energy in the short-time scales band of the radar-derived velocity spectrum might be addressed in future work by modeling the wave field and the radar backscattered signal. It would then be possible to investigate how various parameters of the wave field, e.g. wave height, wave period, wave direction, interact to produce the increased energy levels at super-tidal frequencies.

8. References

Banner, M. L., and D. H. Peregrine, 1993: Wave breaking in deep water. Annu. Rev. Fluid Mech., 25, 373–397.

Banner, M. L., and W. L. Peirson, 1998: Tangential stress beneath wind-driven air-water interfaces. J. Fluid Mech., 364, 115–146.

Banner, M. L. and Phillips, O. M., 1974: On the incipient breaking of small scale waves. J. Fluid Mech., 65, 647-656.

Banner, M. L., A. V. Babanin and I. R. Young, 2000: Breaking probability for dominant waves on the sea surface. J. Phys. Oceanogr., 30, 3145-3160.

Barrick, D. E., 1972: Remote sensing of sea state by radar. Remote Sensing of the Troposphere, V. E. Derr, Ed., U. S. Govt. Printing Office, 194–197.

Barrick, 1986: The role of the gravity-wave dispersion relation in HF radar measurements of the sea surface. IEEE J. Oceanic Eng., OE-11, 286–292.

Barrick, D. E., and B. L. Weber, 1977: On the nonlinear theory for gravity waves on the ocean's surface. Part II: Interpretation and applications. J. Phys. Oceanogr., 7, 11–21.

Barrick, D. E., M. W. Evans, and B. L. Weber. 1977: Ocean surface currents mapped by radar. Science, 198, 138-144.

Chapman, R.D., L.K. Shay, H.C. Graber, J.B. Edson, A. Karachintsev, C.L. Trump, and D.B. Ross, 1997: On the accuracy of HF radar surface current measurements: Intercomparison with ship-based sensors. Journal of Geophysical Research, 102 (C8), 18,737-18,748.

Emery, W. E. and R. E. Thomson, 1997: Data Analysis Methods in Physical Oceanography. Pergamon.

Emery, B. M. , L. Washburn and J. A. Harlan, 2003: Evaluating radial current measurements from CODAR high frequency radars with moored current meters. J. Atmos. Oceanic Technol., accepted.

Graber, H.C., B.K. Haus, R.D. Chapman, and L.K. Shay, 1997: HF radar comparison with moored estimates of current speed and direction: Expected differences and implications. Journal of Geophysical Research, 102 (C8), 18,749-18,766.

Hasselmann, D. E., M. Dunckel and J. A. Ewing, 1980: Directional wave spectra observed during JONSWAP 1973. J. Phys. Oceanogr., 10, 1264-1280.

Huang, N. E., 1979: On surface drift currents in the ocean. J. Fluid Mech., 91, 191-208.

Huang, N. E., Shen, Z., Long, S. R., Wu, M. C., Shih, H. H., Zheng, Q., Yen, N., Tung, C. C., Liu, H. H., 1998: The empirical mode decomposition and the Hilbert spectrum for nonlinear and non-stationary time series analysis. Proc. R. Soc. Lond. A, 454, 903-995.

Huang, N. E., Shen, Z., Long, S. R., 1999: A new view of nonlinear water waves: The Hilbert spectrum., Annu. Rev. Fluid Mech., 31, 417-457.

Jenkins, A. D., 1986: A theory for steady and variable wind- and wave-induced currents. J. Phys. Oceanogr., 16, 1370-1377.

Jenkins, A. D., 1987: Wind and wave induced currents in a rotating sea with depth-varying eddy viscosity. J. Phys. Oceanogr., 17, 938-951.

Kosro, P.M., J.A. Barth, and T.P. Strub, 1997: The coastal jet: Observations of surface currents over the Oregon continental shelf from HF radar. Oceanography, 10 (2), 53-57.

Longuet-Higgins, M. S., 1953: Mass transport in water waves. Philos. Trans. Roy. Soc. London, A245, 535-581.

Longuet-Higgins, M. S., 1983: On the joint distribution of wave periods and amplitudes in a random wave field. Proc. Roy. Soc London, A389, 241-258.

Malone, T. C., 2001: The coastal component of the U.S. integrated ocean observing system. http://www.ocean.us.net/documents.jsp.

Madsen, O. S.,1978: Mass transport in deep water waves. J. Phys. Oceanogr., 8, 1009-1015.

Melville, W. K. and P. Matusov, 2002: Distribution of breaking waves at the ocean surface. Nature, 417, 58-63.

O'Reilly, W. C., R. T. Guza, and R. J. Seymour, 2000: Wave prediction in the Santa Barbara Channel. Minerals Management Service Fifth Symposium on California Islands., 76-80.

Paduan, J.D., and L.K. Rosenfeld, 1996: Remotely sensed surface currents in Monterey Bay from shore-based HF radar (Coastal Ocean Dynamics Application Radar). J. Geophys. Res., 101 (C9), 20,669-20,686.

Phillips, O. M., 1985: Spectral and statistical properties of the equilibrium range in wind-generated gravity waves. J. Fluid Mech., 156, 505-531.

Phillips, O. M., Posner, F. L. & Hansen, J. P., 2001: High range resolution radar measurements of the speed distribution of breaking events in wind-generated ocean waves: Surface impulse and wave energy dissipation rates. J. Phys. Oceanogr. 31, 450–460.

Pierson, W. J., Jr., and L. Moskowitz, 1964: A proposed spectral form for fully developed wind seas based on the similarity theory of S. A. Kitaigorodskii. J. Geophys. Res., 69, 5181–5190.

Rapp, R., and W. K. Melville, 1990: Laboratory measurements of deep water breaking waves. Philos. Trans. Roy. Soc. London, 331A, 735–780.

Richman, J. G., R. A. de Szoeke and R. E. Davis, 1987: Measurements of near-surface shear in the ocean. J. Geophys. Res., 92(C3), 2851-2858.

Shay, L.K., S.J. Lentz, H.C. Graber, and B.K. Haus, 1998: Current structure variations detected by high-frequency radar and vector-measuring current meters. J. Atmos. Oceanic Technol., 15, 237-256.

Srokosz, M. A., 1986: On the probability of breaking in deep water. J. Phys. Oceanogr., 16, 382–385.

Ursell, F., 1950: On the theoretical form of ocean swell on a rotating earth. Mon. Not. Roy. Astron. Soc, Geophys. Suppl., 6, 1-8.

Weber, J. E., 1983: Steady wind- and wave-induced currents in the open ocean. J. Phys. Oceanogr., 13, 524-530.

Weber, J. E. and A. Melsom, 1993: Volume flux induced by wind and waves in a saturated sea. J. Geophys. Res., 98(C3), 4739-4745.

Weber, B. L., and D. E. Barrick, 1977: On the nonlinear theory for gravity waves on the ocean's surface. Part I: Deviations. J. Phys. Oceanogr., 7, 3–10.

Woodward M. J., W. S. Huggett, and R. E. Thomson, 1990: Near-surface moored current meter intercomparisons. Can. Tech. Report Hydrogr. And Ocean Sci., No. 125, Dept. Fish. Oceans.

Wyatt, L. R., 1990: A relaxation method for integral inversion applied to HF radar measurement of the ocean wave directional spectrum. Intl. J. Remote Sens., 11, 1481-1494.

Wyatt, L. R., 1991: High-frequency radar measurements of the ocean wave-directional spectrum. IEEE J. Oceanic Eng., 16, 1, 163-169.

Wyatt, L. R., 1995: High order nonlinearities in HF radar backscattering from the ocean surface. IEE Proc. Radar, Sonar Navig., 142, 293–300.

Wyatt, L. R. and J. J. Green, 2002: The availability and accuracy of HF radar wave measurements. Proceedings, International Geoscience and Remote Sensing Symposium, Toronto, Canada.

Xu and Bowen, 1994: Wave- and wind-driven flow in water of finite depth. J. Phys. Oceanogr., 24, 1850-1866.

9. List of Acronyms

ADCP	Acoustic Doppler Current Profiler
ARG	Pt. Arguello Radar Site
CDIP	Coastal Data Information Program of Scripps Institution of Oceanography
CM	Current Meter
CMM1	Time Series of Current Meter After Removal of IMF1
DF	Direction-Finding
EDOF	Effective Degrees of Freedom
EMD	Empirical Mode Decomposition
EOF	Empirical Orthogonal Functions
FBK	Fallback 22 Radar Site
FMCW	Frequency Modulation-Continuous Wave
FMICW	Frequency Modulation-Interrupted Continuous Wave
HF	High Frequency as in HF Radar
HFM1	Time Series of HF Radar After Removal of IMF1
IMF	Intrinsic Mode Function
IMF1	Intrinsic Mode Function 1 which corresponds to the shortest time scale motions of a time series; used interchangeably with "SI"
JONSWAP	JOint North Sea WAve Project
RFI	Radio Frequency Interference
RFG	Refugio State Park Radar Site
SBC	Santa Barbara Channel
SI	Standard Deviation of an IMF1 Time Series
SNR	Signal-to-Noise Ratio
STD	Standard Deviation
VMCM	Vector-Measuring Current Meter